

The low density and magnetization of a massive galaxy halo exposed by a fast radio burst

J. Xavier Prochaska^{1,2}, Jean-Pierre Macquart³, Matthew McQuinn⁴,
Sunil Simha¹, Ryan M. Shannon⁵, Cherie K. Day^{5,6},
Lachlan Marnoch^{6,7}, Stuart Ryder⁷, Adam Deller⁵, Keith W. Bannister⁶,
Shivani Bhandari⁶, Rongmon Bordoloi⁸, John Bunton⁶,
Hyerin Cho⁹, Chris Flynn⁵, Elizabeth K. Mahony⁶,
Chris Phillips⁶, Hao Qiu¹⁰, Nicolas Tejos¹¹

1: University of California Observatories-Lick Observatory, University of California, 1156 High Street, Santa Cruz, CA 95064, USA

2: Kavli Institute for the Physics and Mathematics of the Universe, 5-1-5 Kashiwanoha, Kashiwa, 277-8583, Japan

3: International Centre for Radio Astronomy Research, Curtin University, Bentley WA 6102, Australia

4: Astronomy Department, University of Washington, Seattle, WA 98195, USA

5: Centre for Astrophysics and Supercomputing, Swinburne University of Technology, Hawthorn VIC 3122, Australia

6: Commonwealth Science and Industrial Research Organisation, Australia Telescope National Facility, P.O. Box 76, Epping, NSW 1710 Australia

7: Department of Physics and Astronomy, Macquarie University, NSW 2109, Australia

8: North Carolina State University, Department of Physics, Raleigh, NC 27695-8202, USA

9: School of Physics and Chemistry, Gwangju Institute of Science and Technology, Gwangju, 61005, Korea

10: Sydney Institute for Astronomy, School of Physics, University of Sydney, Sydney, NSW 2006, Australia

11: Instituto de Física, Pontificia Universidad Católica de Valparaíso, Casilla 4059, Valparaíso, Chile

*To whom correspondence should be addressed; E-mail: xavier@ucolick.org.

Present-day galaxies are surrounded by cool and enriched halo gas extending to hundreds of kiloparsecs. This halo gas is thought to be the dominant reservoir of material available to fuel future star formation, but direct constraints on its mass and physical properties have been difficult to obtain. We report the detection of a fast radio burst (FRB 181112) with arcsecond precision, which passes through the halo of a foreground galaxy. Analysis of the burst shows the halo gas has low net magnetization and turbulence. Our results imply predominantly diffuse gas in massive galactic halos, even those hosting active supermassive black holes, contrary to some previous results.

The low-density gas located in the outskirts of galaxies influences the process of galaxy formation, especially gas accretion and feedback (1). Absorption-line spectroscopy can detect this nearly invisible medium. Surveys demonstrate a very high incidence of cool gas (with temperature $T \sim 10^4$ K), detected through hydrogen Lyman series and continuum absorption, surrounding galaxies with masses similar to our Milky Way (e.g. (1, 2)). Properties of this gas depend on galaxy mass but are otherwise insensitive to the galaxy's internal properties (1, 3–5). Estimates for the total mass of the cool gas match or exceed the baryonic mass of the galaxy (4, 6). Theoretical treatments of halo gas around present-day galaxies disagree on the proportion of total mass retained in the halo during galaxy formation, with estimates ranging from several tens of percent to all of the baryons predicted to accrete into the halo (e.g. (7, 8)). This uncertainty stems from observational insensitivity to the hot ($T \gtrsim 10^6$ K) gas which pervades galaxy halos (and within which the cold gas is embedded), and from systematic uncertainties in estimating its mass (1, 6). Constraints on the density and temperature of the halo gas are sufficiently limited to allow qualitatively different descriptions of its ionization and distribution (9, 10). The origin of the cool gas and its composition are challenging to explain theoretically; some models require cosmic rays and magnetic fields to transport material from the central galaxy to sustain the cool

medium (e.g. (11)).

At Coordinated Universal Time 17:31:15.48365 on 2018 Nov 12 the Commensal Real-time ASKAP Fast Transients (CRAFT) survey on the Australian Square Kilometer Array Pathfinder (ASKAP) detected a fast radio burst (FRB 181112) from the 12 antennas observing at the time. The burst arrival time swept across the observing band ($\approx 1.129 - 1.465$ GHz, Fig. 1A) due to propagation of the burst through the foreground plasma. The burst sweep yields an estimate of the FRB dispersion measure $DM_{\text{FRB}} = 589.27 \pm 0.03 \text{ pc cm}^{-3}$ which is the integrated density of electrons n_e at distance r from Earth scaled by $(1+z)^{-1}$ with z the redshift: $DM_{\text{FRB}} \equiv \int n_e / (1+z) dr$. The real-time detection triggered full download of the voltage data; these precisely localized the burst to a sky position 21h49m23.630s, $-52^{\circ}58'15.39''$ (right ascension, declination, J2000) with a statistical (systematic) error ellipse oriented at 120 deg E of N on the sky with major axis $a = 0.555''(3.2'')$ and minor axis $b = 0.153''(0.8'')$ (12).

Fig. 1B shows a g -band image centered on FRB 181112 obtained with the FOcal Reducer/low dispersion Spectrograph 2 (FORS2) instrument on the Very Large Telescope (VLT). It shows the presence of a galaxy coincident with FRB 181112, previously cataloged by the Dark Energy Survey (DES; (13)) as DES J214923.66–525815.28. The DES and FORS2 data also show a luminous galaxy $\approx 5''$ to the North of the FRB event (DES J214923.89–525810.43). We used follow-up spectroscopy with the FORS2 instrument to measure the redshift (12) of the former galaxy as $z = 0.47550$, and the latter galaxy as $z = 0.3674$, i.e. in the foreground. We associate FRB 181112 with DES J214923.66–525815.28. Compared to the other three known host galaxies of FRBs, the host galaxy of FRB 181112 has an intermediate stellar mass of $M_{\star} \approx 10^{9.4}$ solar masses (M_{\odot}) (Fig. S3; (12)). It has colors matching star-forming galaxies at $z \sim 0.4$, has an estimated star formation rate of $0.6 M_{\odot} \text{ yr}^{-1}$, and shows no signatures of an active galactic nucleus (AGN) (12).

The FRB sightline passes at an impact parameter $R_{\perp} = 29 \text{ kpc}$ from DES J214923.89–525810.43

(hereafter referred to as FG-181112) allowing us to probe the halo of this foreground galaxy. We analyzed the DES, FORS2, and complementary longer-wavelength Wide-field Infrared Survey Explorer (WISE) data to determine FG-181112’s physical properties (12). We derive a high stellar mass $\log_{10} M_{\star}/M_{\odot} = 10.69^{+0.22}_{-0.46}$, nebular emission lines indicative of an AGN and classifying it as a Seyfert galaxy, and an old (> 1.4 Gyr) quiescent stellar population (Tables 1 and S5). Surveys of the halo gas surrounding galaxies of similar mass, with or without AGN activity (14), almost ubiquitously reveal strong cool ($T \sim 10^4$ K) gas absorption for sightlines $R_{\perp} \leq 100$ kpc. Generally, the inferred total column densities of ionized gas exceed 10^{20} cm^{-2} (4, 6), and transitions of heavy elements indicate a turbulent velocity field (15) suggesting that a fraction of the gas has a relatively high density ($n_{\text{H}} \sim 1 \text{ cm}^{-3}$; (16)). Such a foreground medium should impact the FRB signal.

The column of gas close to this massive galaxy, however, does not dominate DM_{FRB} . It contributes only $\text{DM}_{\text{FG}} \sim 50 - 120 \text{ pc cm}^{-3}$, depending on assumptions for the density profile and total mass of the halo gas (12). The measured DM_{FRB} is consistent with models that include cosmic gas, our Galaxy, and the host (Fig. S9; (17, 18)). The sightline to FRB 181112 also intersects the edge of the Fermi Bubbles (12), a complex of hot gas encompassing the Galactic center. The expected DM contribution from gas in these bubbles is small (12), but their entrained magnetic field may contribute to the FRB rotation measure.

The rotation measure RM is the density-weighted integral of the magnetic field parallel to the FRB sightline. The voltages recorded from the ASKAP antennas measure the electric field at the antenna locations in two orthogonal directions on the plane of the sky, enabling the linear polarization fraction of the burst radiation (and its position angle) to be measured as a function of frequency. Averaged over its duration we find the burst to be approximately 90% linearly polarized and 10% circularly polarized (12). This can be used to estimate the burst RM, as $\text{PA}_{\text{obs}} = \text{PA}_{\text{int}} + (c/\nu)^2 \text{RM}$, where ν is the frequency and PA_{obs} and PA_{int} are the

observed and intrinsic polarization angles, respectively. Fig. 2 depicts the frequency sweep of the polarization angle; the apparent ν^{-2} frequency dependence is the RM signature. We fitted an RM to the sweep, yielding $\text{RM} = 10.9 \pm 0.9 \text{ rad m}^{-2}$. This is a low RM value, consistent (within the uncertainty) to the estimated RM due to our Galaxy towards FRB 181112 (12). Adopting an upper limit of $\text{RM} < 11 \text{ rad m}^{-2}$, we calculate an upper limit for the maximum parallel magnetic field $B_{\parallel}^{\text{max}}$ in the halo of FG-181112, $B_{\parallel}^{\text{max}} < 0.8 \mu\text{G} (n_e/10^{-3} \text{ cm}^{-3})^{-1} (\Delta L/30 \text{ kpc})^{-1}$ in the limit of a perfectly ordered magnetic field with ΔL a characteristic length-scale through the halo. We have adopted fiducial values for n_e and L that may characterize the halo of FG-181112 (similar to those adopted for the DM_{FG} estimation). Field reversals would lead us to underestimate $B_{\parallel}^{\text{max}}$. Nevertheless, this low value for $B_{\parallel}^{\text{max}}$ implies that either the magnetic field in the halo is low compared to the interstellar medium, or that it is largely disordered.

These constraints have implications for the circumgalactic gas. The magnetic field value in equipartition with the thermal energy of the virialized halo gas is $B_{\text{eq}} \equiv \sqrt{8\pi n_e k_b T} = 2 \mu\text{G} (n_e/10^{-3} \text{ cm}^{-3})^{1/2} (T/10^6 \text{ K})^{1/2}$ with k_b the Boltzman constant. Our $B_{\parallel}^{\text{max}}$ limit is comparable to B_{eq} for physically motivated n_e , ΔL and T , constraining the magnetic field to be near or below equipartition if the total field is comparable to the net parallel field. Magnetic fields around the equipartition value enhance the rate of condensation of the hot circumgalactic gas into cooler clouds (11) as well as the survival of cool accreting gas (19). Near equipartition field strengths are generated in some models in which cosmic ray pressure transports cool gas and metals to large distances from galaxies (20, 21). Our limit on $B_{\parallel}^{\text{max}}$ is below the mean estimate for sightlines that show strong gas absorption (22) despite our sightline likely intersecting gas with similarly strong absorption in FG-181112 (e.g. (3)).

The halo gas of FG-181112 broadens the width of the pulse at any given frequency. This temporal broadening τ_{scatt} arises from density fluctuations within the medium which impose small light-travel differences for rays propagating through the gas (17, 23). This scattering is

geometrical and its effects are maximal for a scattering ‘screen’ located at one-half the distance to the FRB. We determine an upper limit of $\tau_{\text{scatt}} < 40 \mu\text{s}$ due to scattering, constraining both the turbulent properties of the halo gas and its density. A pulse with 150 times higher width (3 ms) would have still been detected, i.e. the very narrow width of FRB 181112 is not the result of observational bias. Fig. 2B shows that the temporal profile of FRB 181112 consists of two pulses separated by approximately $800 \mu\text{s}$. The broadening limit is derived by modeling each component as a symmetric intrinsic pulse convolved with the one-sided exponential decay expected due to scattering (see (12)). Temporal smearing due to inhomogeneities in the plasma distribution along the line of sight would otherwise broaden the pulse to a frequency-dependent duration $\tau_{\text{scatt}}(\nu) = \tau_0(\nu/1 \text{ GHz})^\gamma$, where the index γ is typically ≈ -4 (12).

The observed τ_{scatt} constrains the integral of the square of the density along the sight-line, $\int dx \delta n_e(x)^2$, which we relate to the electron column density with the parameterization $\langle n_e \rangle \Delta L^{1/2} = \alpha^{-1} \left(\int dx \delta n_e^2 \right)^{1/2}$, which takes the halo of FG-181112 to have characteristic length ΔL with an average density of $\langle n_e \rangle$. Thus, the parameter α encapsulates the root-mean-square amplitude of density fluctuations and the volume filling fraction of the turbulence, f_V . The limit on the in situ density assuming a Kolmogorov spectrum of turbulence (12) is

$$\langle n_e \rangle < 2 \times 10^{-3} \alpha^{-1} \left(\frac{\Delta L}{50 \text{ kpc}} \right)^{-1/2} \left(\frac{L_0}{1 \text{ kpc}} \right)^{1/3} \left(\frac{\tau_{\text{scatt}}}{40 \mu\text{s}} \right)^{5/12} \text{ cm}^{-3}, \quad (1)$$

where $\Delta L \sim 50 \text{ kpc}$ approximates the path length through the foreground halo and L_0 is the outer scale of turbulence. As the turbulence is likely to be sourced by galactic winds and inflows, we expect it to be driven at scales less than the impact parameter ($\sim 30 \text{ kpc}$) and consider $L_0 = 1 \text{ kpc}$ a reasonable value.

We now examine two standard models for halo gas in which the medium is comprised of either hot ($T \sim 10^6 \text{ K}$) virialized gas or cool gas pressure-confined by the hot gas. In the case of hot virialized gas, our constraint on $\langle n_e \rangle$ suggests densities lower than those expected of

$\sim 10^{-3} \text{ cm}^{-3}$ gas with kiloparsec driving scales (see Fig. S12). Because we expect the volume filling factor of this gas to be near unity, the upper limit on the density can only be ameliorated if the gas is much less turbulent (i.e. $\alpha \ll 1$) relative to galactic astrophysical plasmas, especially the interstellar medium of our Galaxy, where $\alpha \sim 7$ (12, 24).

For turbulent, cool 10^4K clouds embedded in a hot medium, the constraints are stronger. Assuming pressure equilibrium with characteristic values for the hot gas $n_e = 10^{-3} \text{ cm}^{-3}$ and $T = 2 \times 10^6 \text{ K}$, application of equation (1) with $L_0 = 1 \text{ kpc}$ and $\Delta L = 50 \text{ kpc}$ yields $\alpha < 0.01$. Since $\alpha \propto f_V^{1/2}$, we require a filling factor of cool clouds of $f_V < 10^{-4}$ if the clouds are fully turbulent. Even lower values are required to satisfy this condition if the driving for turbulence within cool clouds is instead at parsec scales, which may be physically motivated (25).

These limits on the halo gas density derived from the scattering analysis contradict prior inferences that cool halo gas has a volume filling fraction of $f_V \sim 10^{-3} - 10^{-2}$ (6, 26, 27). The total neutral hydrogen column density offers the most direct comparison to our result: photoionization equilibrium constrains the same combination of parameters as scattering, implying $(n_e/0.1 \text{ cm}^{-3}) (f_V/10^{-3})^{1/2} (\Delta L/50 \text{ kpc})^{1/2} \sim 1$ if we take a typical neutral hydrogen column density of 10^{18} cm^{-2} at 30 kpc measured for halos with similar masses as FG-181112 (4). Reconciling these values with the scattering from FG-181112 either implies that the cool clouds are less turbulent than assumed or that our sight line has less cool gas than is typical. The foreground galaxy is classified as a Seyfert, with an embedded accreting supermassive black hole in a central AGN that could lead to a more evacuated halo (28), although it has been argued that such activity may lead to more cool gas (29). Even if the clouds are not turbulent and instead we consider the refractive bending of light through a network of parsec-scale clouds (25), we rule out a population of 0.1 pc clouds or smaller with $f_V \sim 10^{-3}$ (12).

FRBs experience a number of propagation effects which render them sensitive probes of the density, magnetic field and turbulence of the otherwise elusive gas that pervades galaxy halos.

The constraints derived from FRB 181112 for the halo of a massive galaxy are summarized in Fig. 3. The n_e, B_{\parallel} parameter space ruled out by our observations conflicts with several previous inferences for halo gas (22, 26, 27). Our observations indicate a density of hot gas that is lower than in many models and also a column of cool gas that is smaller than commonly inferred.

These results establish intergalactic optics as a potent means of elucidating the physical properties of the diffuse gas in the halos of galaxies. It may further be that the multiple pulses observed in FRB 181112 are due to multipath propagation through the gas. This would be a natural consequence of a medium comprising very low filling-factor cool clouds embedded in hot virialized halo gas, with the pulse multiplicity signifying the number of clouds intersected, and their arrival times yielding their offsets from the direct burst sight line. This work represents only the first step in harnessing the impulsive properties of FRBs to resolve the structures of galaxy halos.

References

1. J. Tumlinson, M. S. Peeples, J. K. Werk, *Annu. Rev. Astron. Astrophys.* **55**, 389 (2017).
2. J. X. Prochaska, B. Weiner, H.-W. Chen, J. Mulchaey, K. Cooksey, *Astrophys. J.* **740**, 91 (2011).
3. C. Thom, *et al.*, *Astrophys. J.* **758**, L41 (2012).
4. J. X. Prochaska, *et al.*, *Astrophys. J.* **837**, 169 (2017).
5. R. Bordoloi, *et al.*, *Astrophys. J.* **864**, 132 (2018).
6. J. K. Werk, *et al.*, *Astrophys. J.* **792**, 8 (2014).
7. Z. Hafen, *et al.*, *Mon. Not. R. Astro. Soc.* **488**, 1248 (2019).

8. A. Pillepich, *et al.*, *Mon. Not. R. Astro. Soc.* **473**, 4077 (2018).
9. Y. Faerman, A. Sternberg, C. F. McKee, *Astrophys. J.* **835**, 52 (2017).
10. J. Stern, *et al.*, *Astrophys. J.* **865**, 91 (2018).
11. S. Ji, S. P. Oh, M. McCourt, *Mon. Not. R. Astro. Soc.* **476**, 852 (2018).
12. Materials and methods are available as supplementary materials .
13. T. M. C. Abbott, *et al.*, *Astrophys. J.* **239**, 18 (2018).
14. T. A. M. Berg, *et al.*, *Mon. Not. R. Astro. Soc.* **478**, 3890 (2018).
15. H.-W. Chen, *et al.*, *Astrophys. J.* **724**, L176 (2010).
16. T.-W. Lan, H. Mo, *Mon. Not. R. Astro. Soc.* **486**, 608 (2019).
17. M. McQuinn, *Astrophys. J.* **780**, L33 (2014).
18. J. X. Prochaska, Y. Zheng, *Mon. Not. R. Astro. Soc.* **485**, 648 (2019).
19. T. Berlok, C. Pfrommer, *Mon. Not. R. Astro. Soc.* **485**, 908 (2019).
20. R. Pakmor, C. Pfrommer, C. M. Simpson, V. Springel, *Astrophys. J.* **824**, 30 (2016).
21. I. S. Butsky, T. R. Quinn, *Astrophys. J.* **868**, 108 (2018).
22. M. L. Bernet, F. Miniati, S. J. Lilly, P. P. Kronberg, M. Dessauges-Zavadsky, *Nature* **454**, 302 (2008).
23. J.-P. Macquart, J. Y. Koay, *Astrophys. J.* **776**, 125 (2013).

24. K. R. Anantharamaiah, R. Narayan, *Radio Wave Scattering in the Interstellar Medium*, J. M. Cordes, B. J. Rickett, D. C. Backer, eds. (1988), vol. 174 of *American Institute of Physics Conference Series*, pp. 185–189.
25. M. McCourt, S. P. Oh, R. O’Leary, A.-M. Madigan, *Mon. Not. R. Astro. Soc.* **473**, 5407 (2018).
26. S. Cantalupo, F. Arrigoni-Battaia, J. X. Prochaska, J. F. Hennawi, P. Madau, *Nature* **506**, 63 (2014).
27. T.-W. Lan, M. Fukugita, *Astrophys. J.* **850**, 156 (2017).
28. E. Choi, J. P. Ostriker, T. Naab, L. Oser, B. P. Moster, *Mon. Not. R. Astro. Soc.* **449**, 4105 (2015).
29. L. P. David, *et al.*, *Astrophys. J.* **792**, 94 (2014).
30. ATCA dataset. <https://doi.org/10.25919/5d7e19c34743c>
31. FRB repository. <http://doi.org/10.5281/zenodo.3403651>
32. Planck Collaboration, *et al.*. Planck 2015 results. XIII. Cosmological parameters. *Astron. & Astrophys.* **594**, A13 (2016).
33. K. W. Bannister, *et al.*, *Science* **365**, 565 (2019).
34. A. T. Deller, *et al.*, *Pub. Astron. Soc. Pacific* **123**, 275 (2011).
35. E. W. Greisen, *Information Handling in Astronomy - Historical Vistas*, A. Heck, ed. (2003), vol. 285 of *Astrophysics and Space Science Library*, p. 109.

36. M. Kettenis, H. J. van Langevelde, C. Reynolds, B. Cotton, *Astronomical Data Analysis Software and Systems XV*, C. Gabriel, C. Arviset, D. Ponz, S. Enrique, eds. (2006), vol. 351 of *Astronomical Society of the Pacific Conference Series*, p. 497.
37. J. P. McMullin, B. Waters, D. Schiebel, W. Young, K. Golap, *Astronomical Data Analysis Software and Systems XVI*, R. A. Shaw, F. Hill, D. J. Bell, eds. (2007), vol. 376 of *Astronomical Society of the Pacific Conference Series*, p. 127.
38. R. J. Sault, P. J. Teuben, M. C. H. Wright, *Astronomical Data Analysis Software and Systems IV*, R. Shaw, H. Payne, J. J. E. Hayes, eds. (1995), vol. 77 of *Astronomical Society of the Pacific Conference Series*, p.433.
39. J. E. Everett, J. M. Weisberg, *Astrophys. J.* **553**, 341 (2001).
40. F. Feroz, M. P. Hobson, M. Bridges, *Mon. Not. R. Astro. Soc.* **398**, 1601 (2009).
41. E. L. Wright, *et al.*. The Wide-field Infrared Survey Explorer (WISE): Mission Description and Initial On-orbit Performance. *Astron. J.* **140**, 1868 (2010).
42. I. Appenzeller, *et al.*, *The Messenger* **94**, 1 (1998).
43. G. Berriman, J. Good, *Publ. Astron. Soc. Pac.* **129**, 058006 (2017).
44. D. Lang, *et al.*, *Astron. J.* **139**, 1782 (2010).
45. E. Bertin, S. Arnouts, *Astron. Astrophys. Suppl. Ser.* **117**, 393 (1996).
46. PyPEIT, The Python Spectroscopic Data Reduction Pipeline. <https://pypeit.readthedocs.io>
47. E. Platts, *et al.*, *arXiv e-prints* arXiv:1810.05836 (2018).

48. S. Noll, *et al.*, *Astron. & Astrophys.* **507**, 1793 (2009).
49. G. Bruzual, S. Charlot, *Mon. Not. R. Astro. Soc.* **344**, 1000 (2003).
50. D. Calzetti, *et al.*, *Astrophys. J.* **533**, 682 (2000).
51. D. A. Dale, *et al.*, *Astrophys. J.* **784**, 83 (2014).
52. M. Cappellari, *Mon. Not. R. Astro. Soc.* **466**, 798 (2017).
53. L. J. Kewley, M. A. Dopita, R. S. Sutherland, C. A. Heisler, J. Trevena, *Astrophys. J.* **556**, 121 (2001).
54. G. Kauffmann, *et al.*, *Mon. Not. R. Astro. Soc.* **346**, 1055 (2003).
55. R. Cid Fernandes, *et al.*, *Mon. Not. R. Astro. Soc.* **403**, 1036 (2010).
56. S. P. Tendulkar, *et al.*, *Astrophys. J.* **834**, L7 (2017).
57. V. Ravi *et al.*, *Nature* **572**, 352 (2019).
58. J. Moustakas, *et al.*, *Astrophys. J.* **767**, 50 (2013).
59. M. Nicholl, *et al.*, *Astrophys. J.* **843**, 84 (2017).
60. C. Y. Peng, L. C. Ho, C. D. Impey, H.-W. Rix, *Astron. J.* **139**, 2097 (2010).
61. L. Bradley, *et al.*, 10.5281/zenodo.2533376
62. B. P. Moster, *et al.*, *Astrophys. J.* **710**, 903 (2010).
63. J. DeRose, *et al.*, *Astrophys. J.* **875**, 69 (2019).
64. J. M. Cordes, T. J. W. Lazio, *arXiv e-prints* arXiv:astro-ph/0207156 (2002).

65. J. Navarro, C. Frenk, S. White, *Astrophys. J.* **490**, 493 (1997).
66. D. Fielding, E. Quataert, M. McCourt, T. A. Thompson, *Mon. Not. R. Astro. Soc.* **466**, 3810 (2017).
67. M. Su, T. R. Slatyer, D. P. Finkbeiner, *Astrophys. J.* **724**, 1044 (2010).
68. R. Bordoloi, *et al.*, *Astrophys. J.* **834**, 191 (2017).
69. M. T. Karim, *et al.*, *Astrophys. J.* **860**, 98 (2018).
70. E. Carretti, *et al.*, *Nature* **493**, 66 (2013).
71. N. Oppermann, *et al.*, *Astron. & Astrophys.* **542**, A93 (2012).
72. A. H. Maller, J. S. Bullock, *Mon. Not. R. Astro. Soc.* **355**, 694 (2004).
73. A. Woodfinden, R.N. Henriksen, J. Irwin, S.C. Mora-Partiarroyo, *Mon. Not. R. Astro. Soc.* **487**, 1498 (2019).
74. W. A. Coles, R. G. Frehlich, B. J. Rickett, J. L. Codona, *Astrophys. J.* **315**, 666 (1987).
75. J. W. Armstrong, B. J. Rickett, S. R. Spangler, *Astrophys. J.* **443**, 209 (1995).
76. L. C. Lee, J. R. Jokipii, *Astrophys. J.* **201**, 532 (1975).
77. M. McQuinn, J. K. Werk, *Astrophys. J.* **852**, 33 (2018).
78. Y. Lithwick, P. Goldreich, *Astrophys. J.* **562**, 279 (2001).
79. P. Goldreich, S. Sridhar, *Astrophys. J.* **438**, 763 (1995).
80. M. McCourt, P. Sharma, E. Quataert, I. J. Parrish, *Mon. Not. R. Astro. Soc.* **419**, 3319 (2012).

81. H. K. Vedantham, E. S. Phinney, *Mon. Not. R. Astro. Soc.* **483**, 971 (2019).
82. B. T. Draine, *Physics of the Interstellar and Intergalactic Medium* (2011).
83. J. S. Morgan, *et al.*, *Astrophys. J.* **768**, 12 (2013).
84. S. R. Spangler, C. R. Gwinn, *Astrophys. J.* **353**, L29 (1990).
85. W. Farah, *et al.*, *Mon. Not. R. Astro. Soc.* **478**, 1209 (2018).
86. M. Ackermann, *et al.*, *Astrophys. J.* **793**, 64 (2014).

Acknowledgments

Based on observations collected at the European Southern Observatory under ESO programme 0102.A-0450(A). We are grateful to Australia Telescope National Facility (ATNF) operations staff and the Murchison Radio-astronomy Observatory staff for supporting our ASKAP operations, and the ATNF Director and Steering Committee for dedicating time for these observations. K.W.B., J.P.M, and R.M.S. acknowledge Australian Research Council (ARC) grant DP180100857. A.T.D. is the recipient of an ARC Future Fellowship (FT150100415). R.M.S. acknowledges support through ARC grants and CE170100004. N.T. acknowledges support from PUCV research funding 039.333/2018. Work at the Naval Research Laboratory is supported by NASA. The Australian Square Kilometre Array Pathfinder, Australia Telescope Compact Array, and Parkes Radio Telescope are part of the Australia Telescope National Facility which is managed by CSIRO. Operation of ASKAP is funded by the Australian Government with support from the National Collaborative Research Infrastructure Strategy. ASKAP uses the resources of the Pawsey Supercomputing Centre. Establishment of ASKAP, the Murchison Radio-astronomy Observatory and the Pawsey Supercomputing Centre are initiatives of the

Australian Government, with support from the Government of Western Australia and the Science and Industry Endowment Fund. We acknowledge the Wajarri Yamatji as the traditional owners of the Murchison Radio-astronomy Observatory site.

Funding

J.X.P. and S.S. are supported by the National Science Foundation grant AST-1911140. K.W.B., J.P.M, and R.M.S. acknowledge Australian Research Council (ARC) grant DP180100857. A.T.D. is the recipient of an ARC Future Fellowship (FT150100415). R.M.S. acknowledge support through ARC grant FL150100148 and through ARC grant CE170100004. N.T. acknowledges support from PUCV research funding 039.333/2018.

Author contributions

J.X.P., J.P.M., M.M., S.S., R.M.S, C.F., and C.K.D drafted the manuscript. J.X.P., N.T., S.R., L.M, S.S., and E.M. obtained, reduced and interpreted optical observations. R.B. did the *FERMI* bubble analysis. K.W.B. built the search and voltage capture software. A.D., C.P., C.K.D. H.C.,H.Q. and S.B., designed, built and conducted the correlation, calibration and imaging software to localize FRB 181112. R.M.S. led the ASKAP observing, and interpreted radio band polarization data. E.M. and S.B. and obtained, reduced, and interpreted ATCA data. J.B. designed the ASKAP digital systems.

Competing Interests

The authors declare no competing interests.

Data and materials availability:

Based on observations collected at the European Southern Observatory under ESO programs 0102.A-0450(A) and 2102.A-5005(A) (PI: Macquart), available from <http://archive.>

eso.org/. Observations from the Australia Telescope Compact Array under program C3211 (PI: Shannon), and the Parkes radio telescope under program P958 (PI: Shannon) can be retrieved from <https://atoa.atnf.csiro.au/>.

Further datasets used in this paper are available from the gSTAR Data Management and Collaboration Platform (gDMCP) at <https://data-portal.hpc.swin.edu.au/> using the tag FRB181112 : nine visibility data sets used to calibrate and determine the localisation of FRB 181112, radio images of the FRB and the surrounding field, and the ATCA images used for astrometric alignment.

Data reduction scripts and code written by the co-authors for this project are available from the CRAFT git repository <https://bitbucket.csiro.au/scm/craf/craft.git>, the PSRVLBIREDUCE repository <https://github.com/dingswin/psrvlbireduce>, the FRB repository <https://github.com/FRBs/FRB>, and the PYPEIT repository <https://github.com/pypeit/pypeit>.

Supplementary Materials:

This PDF file includes

Materials and Methods

Supplementary Text

Figures S1 to S12

Tables S1 to S7

References (30-84)

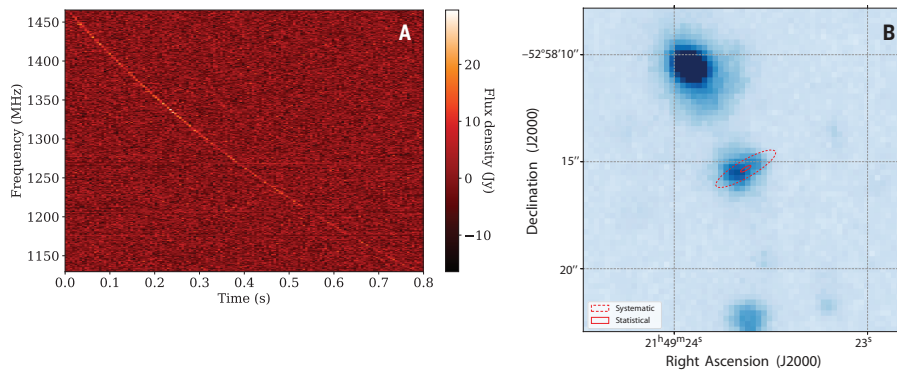


Figure 1:
Dynamic spectrum of FRB 181112 and optical imaging of its host and a coincident foreground galaxy. (A) Dynamic spectrum of FRB 181112 recorded by ASKAP. The dispersion measure $DM_{\text{FRB}} = 589.27 \text{ pc cm}^{-3}$; (B) g -band FORS2 image centered on FRB 181112 whose position is depicted by the red ellipses with solid/dashed lines indicating the statistical/systematic uncertainty. We estimate an additional systematic uncertainty of $\approx 0.5''$ in the astrometric solution of the FORS2 image. The host is well-localized to a faint galaxy cataloged as DES J214923.66–525815.28, and one identifies a brighter galaxy located $\approx 5''$ away at a PA $\approx 13^\circ$ (cataloged as DES J214923.89–525810.43, referred to as FG-181112). The sight-line to FRB 181112 passes through the halo of this foreground galaxy at an impact parameter $R_{\perp} = 29 \text{ kpc}$.

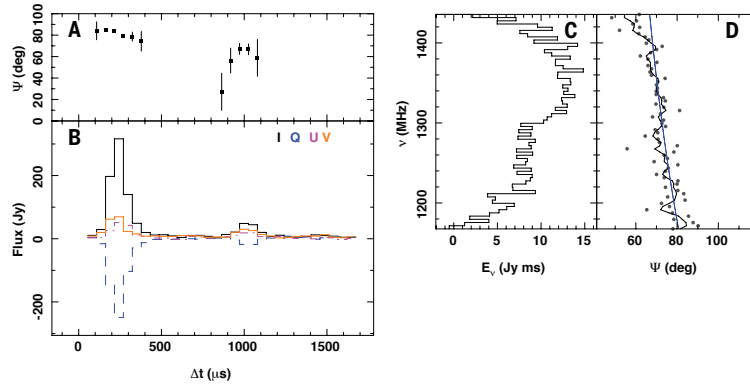


Figure 2:
Spectropolarimetric properties of FRB 181112. A: Relative linear polarization position angle Ψ of the burst averaged in frequency. B: Polarimetric pulse profile of burst in four Stokes components (I - thick solid line; Q - dashed line; U - dashed-dotted line, V - thin solid line). The two components, separated by approximately $800 \mu\text{s}$ show different position angles. C: Spectrum of E_ν burst averaged over both pulses. D: Position angle Ψ of the burst plotted as a function of frequency, with the black points showing measurements in individual frequency channels, and line these measurements smoothed using a Gaussian Kernel with standard deviation of 4 MHz. The variation of the position angle with frequency is the result of Faraday rotation. The blue line shows a maximum-likelihood model for polarization, using the inferred rotation measure $\text{RM} = 10.9 \text{ rad m}^{-2}$.

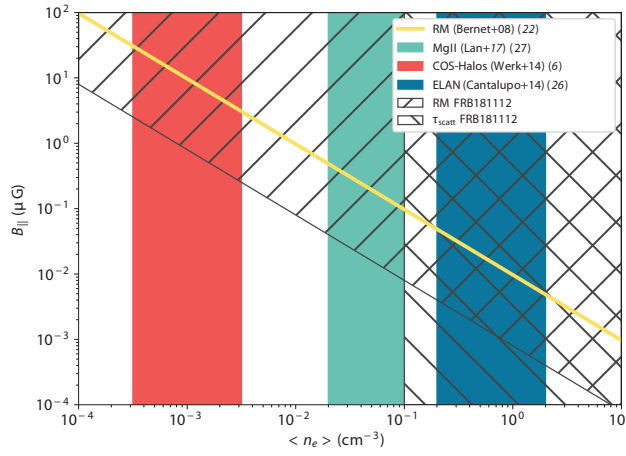


Figure 3: **Constraints on the coherent magnetic field parallel to the line of sight B_{\parallel} and electron density n_e in the halo of FG-181112.** The hatched regions show the parameter space in B_{\parallel} , n_e (cool gas) ruled out for the halo of FG-181112 from the measured RM and τ_{scatt} of FRB 181112. These constraints are largely independent of the properties of the foreground galaxy. We compare these results with previous inferences for the density of cool halo gas (colored regions) based on ionization modeling and Ly α fluorescence. We also illustrate previous estimations for the magnetic field strength in halo gas (yellow curve; (22)) which conflict with our results.

Table 1:

Table 1: **Properties of FRB 181112, its host, and the foreground galaxy FG-181112.**Uncertainties in Right Ascension and Declination are statistical and systematic, as projected onto the RA and Decl. axes. These uncertainties are best described as ellipses with position angle 120 deg East of North and major/minor axes of ($a_{\text{statistical}} = 0.55''$, $b_{\text{statistical}} = 0.15''$) and ($a_{\text{systematic}} = 3.2''$, $b_{\text{systematic}} = 0.8''$). The coherent magnetic field, density and filling factor estimates assume a characteristic path length through the halo of $\Delta L = 50$ kpc. The density and filling factor estimates assume a driving scale with root mean density fluctuations of one at $L_0 = 1$ kpc, with the bound scaling as $\propto L_0^{1/3}$, as well as a Kolmogorov spectrum of turbulence to separations below r_{diff} . The filling factor estimate further assumes cool $T_{\text{cool}} = 10^4$ K gas is in pressure equilibrium with hot gas with density $\langle n_e \rangle = 10^{-3} \text{cm}^{-3}$ and temperature $T_{\text{hot}} = 2 \times 10^6 \text{K}$ hot gas, with the bound scaling as $\propto (\langle n_e \rangle T_{\text{hot}}/T_{\text{cool}})^{-2}$. See (12) and the main text for further details.

FRB	
Right Ascension (J2000)	$327.34846 \pm 0.00007 \pm 0.0006$ deg
Declination (J2000)	$-52.97093 \pm 0.00004 \pm 0.0002$ deg
Dispersion measure (DM_{FRB})	589.27 ± 0.03 pc cm^{-3}
Rotation measure (RM)	10.9 ± 0.9 rad m^{-2}
Pulse width	< 40 μs
Host Galaxy	
Redshift	0.47550 ± 0.00015
Stellar Mass	$2.6 \pm 1.1 \times 10^9 M_{\odot}$
Star formation rate	$0.6 M_{\odot} \text{yr}^{-1}$
Foreground galaxy FG-181112	
Redshift	0.36738 ± 0.00007
Impact parameter to the FRB sightline (R_{\perp})	29 ± 3 kpc
Stellar Mass	$4.9 \pm 3.2 \times 10^{10} M_{\odot}$
Star formation rate	$< 0.3 M_{\odot} \text{yr}^{-1}$
Coherent magnetic field parallel to the line of sight	$B_{\parallel} < 0.5 \mu\text{G} (n_e/10^{-3} \text{cm}^{-3})$
Density constraint for hot, diffuse gas ($f_V \sim 1$)	$n_e < 2 \times 10^{-3} \text{cm}^{-3}$
Filling factor constraint for cool, clumpy gas	$f_V < 10^{-4}$

Supplementary Materials for

The low density and magnetization of a massive galaxy halo exposed by a fast
radio burst

J. Xavier Prochaska, Jean-Pierre Macquart, Matthew McQuinn, Sunil Simha, Ryan M. Shannon, Cherie K. Day, Lachlan Marnoch, Stuart Ryder, Adam Deller, Keith W. Bannister, Shivani Bhandari, Rongmon Bordoloi, John Bunton, Hyerin Cho, Chris Flynn, Elizabeth K. Mahony, Chris Phillips, Hao Qiu, Nicolas Tejos

This PDF file includes

Materials and Methods

Supplementary Text

Figures S1 to S12

Tables S1 to S7

S1 Materials and Methods

Throughout the paper, for calculations that require an assumed cosmology we adopted the model and parameters from the Planck 2015 analysis (32).

S1.1 Data Acquisition and Processing

The ASKAP FRB real-time detection system was configured in an identical manner to that described in (33). At the time of detection of FRB 181112, twelve of the 36 antennas were operational with a maximum baseline of 4392 m.

The method used to determine FRB 181112's astrometric position and uncertainties follows that described in (33). Briefly, four sets of voltage data were captured from the ASKAP telescope. The duration of each voltage data capture was 3.1s and the total bandwidth was 336MHz, comprised of 336×1 MHz complex-sampled dual polarisation sub-bands, with an over-sampling ratio of 32/27 and 4-bit quantisation precision. The voltage captures occurred at the following times and positions, where the positions are the J2000 RA and Decl. at the beam centre:

1. FRB 181112: RA, Decl. = 21h50.0m57.7s, $-53^{\circ}10'32''$, central time UTC 2018-11-12: 17:31:16.6324205+00:00
2. PKS 0407–658 (visit 1), a bright, compact calibrator source: RA, Decl. = 04h08m20.4s, $-65^{\circ}45'09''$, ~5 hours after the FRB [UTC 2018-11-12: 22:30:10.4107085+00:00])
3. PKS 0407–658 (visit 2): RA, Decl. = 04h08m20.4s, $-65^{\circ}45'09''$, central time UTC 2018-11-12: 23:55:04.4360995+00:00)
4. PSR J0834–4510, the Vela pulsar: RA, Decl. = 08h35m20.7s, $-45^{\circ}10'35''$, central time UTC 2018-11-13: 00:43:55.610311+00:00)

The first two voltage datasets were affected by a hardware issue which resulted in the loss of 2.3% of the data from one antenna. Shortly after this issue was discovered, at approximately UTC 2018-11-12: 23:00, some components of the ASKAP hardware were reset in order to fix this issue in further observations. This hardware reset meant that calibration solutions from the PKS 0407–658 (visit 1) dataset could not be applied to the subsequently observed Vela dataset, and accordingly the PKS 0407–658 (visit 2) dataset was also acquired. From these four sets of voltage data, nine visibility datasets were produced using the software correlator package DiFX (34). In the summary below, the time resolution refers to the maximum time difference between the first and last data added into an individual visibility accumulator for a given timestep, while the total effective integration time refers to the total amount of valid data added into all visibility accumulators for the entire correlation. The nine datasets are as follows:

- PKS 0407–658 (visit 1) data, correlation centred at PKS 0407–658 (RA, Decl. = 04h08m20.380s, –65d45′09.08″), time resolution 1.3824 s, total effective integration time 3.1 s, correlator frequency resolution 9.3 kHz (the “FRB calibrator” dataset)
- FRB 181112 data, correlation centred at the approximate FRB position (RA, Decl. = 21h49m20s, –52d58′00″), time resolution 1 ms, total effective integration time 1 ms, correlator frequency resolution 9.3 kHz (“FRB gated” dataset)
- FRB 181112 data, correlation centred on the ASKAP beam centre (RA, Decl. = 21h50m57.69s, –53d10′32.48″), time resolution 1.3824 s, total effective integration time 3.1 s, correlator frequency resolution 9.3 kHz (“FRB continuum field” dataset)
- FRB 181112 data, correlation centred near the final FRB position (RA, Decl. = 21h49m23.6s, –52d58′15.4″), time resolution 54 μ s, total effective integration time 1.62 ms, correlator frequency resolution 18.5 kHz (“FRB high time resolution” dataset)

- FRB 181112 data, correlation centred near on the FRB position (RA, Decl. = 21h49m20s, -52d58'00"), time resolution 21 ms, total effective integration time 16 ms, correlator frequency resolution 9.3 kHz ("FRB radio-frequency interference (RFI) subtraction" dataset)
- FRB 181112 data, correlation centred near on the FRB position (RA, Decl. = 21h49m23.6s, -52d58'15.4"), time resolution 21 ms, total effective integration time 16 ms, correlator frequency resolution 18.5 kHz ("FRB high time resolution RFI subtraction" dataset)
- PKS 0407-658 (visit 2) data, correlation centred at PKS 0407-658 (RA, Decl. = 04h08m20.380s, -65d45'09.08"), time resolution 1.3824 s, total effective integration time 3.1 s, correlator frequency resolution 9.3 kHz ("Vela calibrator" dataset)
- Vela data, correlation centred at the position of Vela (RA, Decl. = 08h35m20.65525s, -45d10'35.1545") time resolution 1.3824 s, total effective integration time 62.3 ms, correlator frequency resolution 9.3 kHz ("Vela" dataset)
- Vela data, correlation centred at the position of Vela (RA, Decl. = 08h35m20.65525s, -45d10'35.1545") time resolution 1.3824 s, total effective integration time 311.5 ms, correlator frequency resolution 9.3 kHz ("Vela RFI subtraction" dataset)

All datasets were averaged after correlation to a frequency resolution of 167 kHz.

PKS 0407-658 was first observed ~ 5 hours after FRB 181112 (vist 1) and again ~ 6.4 hours later (visit 2). The RFI free part of the band (~ 266 MHz and 238 MHz, respectively, concentrated in the upper half of the band) was used to determine antenna-based delays, which were then applied to both the calibrator correlation and the associated target field (FRB 181112, or Vela) correlation. Calibration solutions for all datasets were derived using the *AIPS* (35) tasks FRING and CALIB on their respective calibrator datasets. The instrumental bandpass was corrected using the *AIPS* task CPASS, which interpolates over the RFI flagged region of the band

when deriving these frequency-dependent phase and amplitude corrections.

As described in (33), we produced a second set of visibilities for each of the FRB gated, FRB high time resolution, and Vela datasets, to remove the effects of RFI. These datasets are referred to above as “RFI subtraction” datasets. These visibilities were formed by correlating and integrating over two windows on either side of the “on-pulse” window in time, with a gap between the “on” and “off” pulse regions. In the pulsar binning mode used to produce the FRB and Vela datasets (and their RFI subtraction datasets), the DiFX correlator scales the visibility amplitudes by the bin width. Accordingly, to normalise the two data sets to the same amplitude scale, the RFI subtraction visibilities were scaled by the ratio $t_{\text{on}}/t_{\text{off}}$, where t_{on} and t_{off} are the effective integration times of the on- and off-pulse datasets, respectively. These scaled datasets were then subtracted from their “on-pulse” counterparts to remove any contributions to correlated “on-pulse” visibilities that are approximately constant on timescales of 20 ms (which include both RFI and any background celestial sources). This scaling and subtraction was accomplished via a custom ParselTongue (36) script (UVSUBSCALED.PY).

S1.2 Radio Imaging and Astrometric Position Extraction of FRB 181112 and the field

To determine the FRB position, we imaged the gated FRB dataset in *CASA* (37), using the task *TCLEAN* in widefield, multifrequency synthesis, multiscale mode with natural weighting, producing a 256×256 pixel image with 2.5 arcsec pixels. The FRB 181112 position and its uncertainties were then extracted using the *AIPS* task *JMFIT* on the Stokes I image, producing a detection with a significance of 37σ .

The custom *MIRIAD* (38) script described in (33) was then used to similarly reweight the FRB gated dataset’s visibilities, normalizing the FRB amplitude across the band by up- and down-weighting the brightest and faintest regions, respectively, and adjusting the visibility

weights by the inverse of the amplitude correction. This reweighted dataset was imaged with TCLEAN, using the same settings as the unweighted dataset, and its position and uncertainties determined with JMFIT to be RA, Decl. = $21^{\text{h}}49^{\text{m}}23.63^{\text{s}} \pm 0.05^{\text{s}}$, $-52^{\text{d}}58'15.4'' \pm 0.3''$, with a detection significance of 54σ and offsets in RA and Decl. from the previous, naturally-weighted dataset that are less than the positional uncertainties measured for either weighting scheme.

To determine systematic uncertainty in the ASKAP astrometric positions, the FRB continuum field dataset was flagged to remove visibilities corrupted by RFI or dish shadowing (the FRB was observed at low elevation (14.2 deg), producing shadowing on some very short baselines) and then imaged in CASA. The same TCLEAN settings were used as for the FRB gated dataset, except that a 3000×3000 pixel image with 2.5 arcsec pixels was produced. Six background radio sources were detected, with only one having a significance above 10σ . For each of the detected background sources, we used JMFIT to determine its position and uncertainty in the ASKAP image.

To tie the ASKAP field source positions to the third International Celestial Reference Frame (ICRF3) and to search for any radio continuum emission associated with the FRB host galaxy, a 12-hour observation of the FRB field was carried out with the Australia Telescope Compact Array (ATCA) in the 6B array configuration on 2018 Nov 17 UTC. This included scans of three of the background sources described above (SUMSS 215155–531646, SUMSS 215606–532916, and SUMSS 215036–525538, see Table S1) at 1.1 - 3.1 GHz (with heavy RFI flagging from 1.1 - 1.5 GHz) interleaved with observations of three ATCA calibrators (with only two being used for the final analysis, see Table S2), as well as 4.5 - 8.5 GHz observations centered on the FRB position.

Using multi-frequency synthesis, we combined all of the 4.5 – 8.5 GHz data on the FRB field, producing an image with no detection at the FRB position and a 3σ upper limit of $21 \mu\text{Jy}$.

The 1.1 – 3.1 GHz observations were used to refine the positions of the three ASKAP back-

ground sources. However, SUMSS 215036–525538 was found to be too faint to contribute a substantial constraint on the absolute ASKAP accuracy, while SUMSS 215606–532916 was found to be resolved in the ATCA images, also precluding an accurate positional comparison. Consequently, only SUMSS 215155–531646 was used to estimate any systematic errors in the ASKAP image. The position for SUMSS 215155–531646 has a statistical precision of ~ 10 milliarcseconds, but the position differs by ~ 0.5 arcsec when obtained using PKS B2117–642 versus PKS B2215–508 as the calibrator source (see Table S2.) We use the average of the two positions so obtained as the final estimate of the ATCA position for SUMSS 215155–531646 and take the difference between them as an estimate of the uncertainty on this position. While not negligible, this discrepancy is still small compared to the statistical precision to which the ASKAP position for SUMSS 215155–531646 is measured. The final offset between the ATCA and ASKAP positions for SUMSS 215155–531646 was found to be -0.61 ± 2.15 arcsec in RA and 0.68 ± 1.35 arcsec in Decl. Accordingly, as was the case for FRB 180924 (33), our astrometric checks are consistent with no systematic offsets in the ASKAP astrometry, but the precision to which this is confirmed is much lower than for FRB 180924 due to the fainter background sources and the reduced number of antennas active when the FRB was detected. Combining the FRB measurement error with the estimated systematic uncertainty yields a final FRB position of RA, Decl. = $21^{\text{h}}49^{\text{m}}23.63^{\text{s}} \pm 0.24^{\text{s}}$, $-52^{\text{d}}58'15.4'' \pm 1.4''$. Due to the elongated beam shape, the uncertainty in RA and Decl. is highly correlated for both the statistical and the (dominant) systematic contributions. We report the uncertainty projected onto the RA and Decl. axes as is customary, but Fig. 1 shows the total uncertainty ellipse, as generated by combining in quadrature the statistical and systematic positional uncertainty ellipses from JMFIT. As the source being fitted is unresolved in both cases, the size and position angle of the Gaussian model is approximately that of the ASKAP synthesised beam ($16.5 \times 60.0''$ at p.a. 120 degrees East of North), with the uncertainty ellipse being a scaled version of the model.

S1.3 Spectropolarimetry: calibration and rotation measures

To study the polarimetric properties of the burst (both the spectral variations associated with Faraday rotation and temporal variations) the burst data products needed to be calibrated. The calibration strategy used follows methods developed for the localized ASKAP burst described in (33), which we summarize here.

The largest calibration defect is leakage between Stokes U and V due to an unknown phase Φ_0 and delay $\Delta\tau$ between the two orthogonal linear polarization receptors. We do not attempt to correct for the absolute position angle of the burst on the sky.

We can measure these terms by observing a source with determined polarization properties. As in previous work (33), we used observations of the Vela pulsar (PSR J0835–4510), assuming that it has the following fractional polarization properties (33):

$$\frac{L}{I}(\nu) = \frac{\sqrt{Q^2(\nu) + U^2(\nu)}}{I(\nu)} = 0.95 \quad (\text{S1})$$

$$\frac{V}{I}(\nu) = -0.05 \quad (\text{S2})$$

$$\frac{Q}{I}(\nu) = \frac{L}{I}(\nu) \cos(2\text{PA}(\nu)) \quad (\text{S3})$$

$$\frac{U}{I}(\nu) = \frac{L}{I}(\nu) \sin(2\text{PA}(\nu)), \quad (\text{S4})$$

$$(\text{S5})$$

and the polarization position angle is

$$\text{PA}(f) = 0.09 \text{RM}(\nu_{\text{GHz}}^{-2} - 1.4^{-2}) - \text{PA}_0. \quad (\text{S6})$$

Here PA_0 is the polarization position angle at a reference frequency of 1.4 GHz. Based on Parkes observations reported previously (33), we find $\text{RM} = 40 \pm 1 \text{ rad m}^{-2}$ and $\text{PA}_0 = -0.35 \text{ rad}$.

We can then solve for the leakage terms ($\Phi_0, \Delta\tau$ and Ψ) from the uncorrected fractional

linear polarization:

$$\frac{U'}{I}(\nu) = \frac{L}{I}(\nu) \sin(2\text{PA}(\nu) + \Psi_0 + 2\pi\nu\Delta\tau + \Phi_0) + \frac{V}{I}(\nu) \sin(2\pi\nu\Delta\tau + \Phi_0) \quad (\text{S7})$$

$$\frac{V'}{I}(\nu) = -\frac{L}{I}(\nu) \sin(2\text{PA}(\nu) + \Psi_0 + 2\pi\nu\Delta\tau + \Phi_0) + \frac{V}{I}(\nu) \cos(2\pi\nu\Delta\tau + \Phi_0) \quad (\text{S8})$$

After correcting U and Q for the leakage terms, uncertainties on the relative polarization position angle were determined using standard techniques (39).

S1.3.1 Calculating the rotation measure

Bayesian methodology is used to calculate the rotation measure for the FRB, using the data as calibrated above and a technique applied previously (33). To summarize, we measured the rotation measure by modelling the fractional polarization in the calibrated Q_i and U_i for each channel i .

We model the Stokes parameters $\hat{Q}_{m,i}$ and $\hat{U}_{m,i}$ in each channel i to be

$$\hat{Q}_{m,i} = L_i \cos(2\text{PA}_{\text{FRB}}(\nu_i)) \quad (\text{S9})$$

and

$$\hat{U}_{m,i} = L_i \sin(2\text{PA}_{\text{FRB}}(\nu_i)), \quad (\text{S10})$$

where the position angle is

$$\text{PA}_{\text{FRB}}(\nu_i) = 0.09 \text{RM}_{\text{FRB}} \nu_{i,\text{GHz}}^{-2} + \text{PA}_0, \quad (\text{S11})$$

and L_i is the linearly polarized flux density. We assume that the noise is identical in Q and U , is equal across the band and has a Gaussian distribution.

The likelihood in this case is:

$$\mathcal{L} = \prod_i^{N_c} \frac{1}{2\pi\sigma^2} \exp\left[-\frac{(Q_i - \hat{Q}_{m,i})^2}{2\sigma^2}\right] \exp\left[-\frac{(U_i - \hat{U}_{m,i})^2}{2\sigma^2}\right] \quad (\text{S12})$$

We calculate the posterior probabilities for the parameters (PA_0 , RM_{FRB} , and σ). The total polarized intensities in all channels L_i are nuisance parameters over which we can analytically marginalize, assuming uniform priors. The final likelihood is then

$$\mathcal{L} = \prod_i^{N_c} \frac{1}{2\pi\sigma^2} \exp \left[-\frac{Q_i^2 + U_i^2 - (Q_i \cos(2PA_{\text{FRB}}) + U_i \sin(2PA_{\text{FRB}}))^2}{2\sigma^2} \right]. \quad (\text{S13})$$

We assume uniform priors on PA_0 , RM_{FRB} , and Gaussian priors on τ and Φ_0 , with the means of τ and Φ_0 set to their maximum-likelihood values from the model fitted to the Vela pulsar and the standard deviations set to the best-fitting uncertainties. We sample the posterior distribution using a nested-sampling algorithm (40). We recover $RM_{\text{FRB}} = 10.9 \pm 0.9 \text{ rad m}^{-2}$.

S1.4 Optical and near-infrared Observations

Photometry: We have collated cataloged photometry from the Dark Energy Survey (DES) Data Release 1 (DR1; (13)) and the Wide-field Infrared Survey Explorer (WISE; (41)) all-sky survey of the host galaxy of FRB 181112 and FG-181112 for spectral energy distribution (SED) analyses. These data are listed in Table S3.

We also obtained deeper g and I -band images of the field with the FORS2 imaging spectrograph (42) on the ESO VLT in Service Mode on 2018 Dec 3 UT. Five exposures of 500 s in the g_{HIGH} filter with incremental offsets of $10''$ between each were followed by 5×90 s exposures in the I_{BESS} filter with similar offsets. The Standard Resolution collimator was used with 2×2 binning of the CCD array to yield a pixel scale of $0.25''$ per pixel. Skies were photometric, and the median seeing was $\text{FWHM} \approx 0.6''$.

Standard image processing was performed using version 2.9.1 of the ESO Reflex pipeline. The individual images in each filter were combined with the MONTAGE software package (43). Astrometric calibration was applied using Astrometry.net (44) with a precision of $\approx 0.3''$ when compared to the DES catalog, while photometric calibration was derived from DES DR1 for

the g data, or from the ESO night monitoring data for the I -band. Integrated magnitudes for the host galaxy of FRB 181112 and FG-181112 were then extracted from the images using the `flux_auto` quantity provided by SExtractor 2.19.5 (45). For the host galaxy, we find $g = 22.57 \pm 0.04$ and $I = 21.51 \pm 0.04$; for FG-181112, $g = 21.20 \pm 0.02$ and $I = 19.20 \pm 0.02$. Fig. 1B shows a part of the g -band image.

Spectroscopy: On 2018 Dec 5 UT we obtained a series of three 890 s spectral images of FG-181112 and the host of FRB 181112 with the VLT/FORS2 spectrograph, configured with the GRIS_300I grism and a $1''$ wide slit (full-width half max resolving power, $R_{\text{FWHM}} \approx 660$) oriented at a position angle of 24° to include both galaxies simultaneously. These and associated calibration images were processed with the PyPeIt software package (46) and the spectra were optimally extracted and flux-calibrated with standard procedures. The latter includes a correction to match the flux integrated through the DES r filter to its cataloged magnitude (Table S3). The data were taken at an airmass of ≈ 2 with the slit well away from the parallactic angle, and we have not corrected for losses from differential refraction.

S1.5 Properties of the Host Galaxy of FRB 181112

Although not the primary focus of this manuscript, we report here the properties of the host galaxy as these may constrain progenitor models of FRBs (e.g. (47)). For the radio data, the non-detection of emission in the 4.5 - 8.5 GHz ATCA image corresponds to an upper limit of $L_{(6.5\text{GHz})} < 1.3 \times 10^{22}$ W/Hz. Accordingly, if the host of FRB 181112 were to harbor a persistent radio source of the kind seen co-located with the repeating FRB 121102 (luminosity $\sim 1.8 \times 10^{22}$ W/Hz), it must be fainter than the one associated with FRB 121102.

For the optical data, Fig. S1 shows the best fit SED to the DES photometry of the host galaxy (Table S3) performed with the CIGALE software package (48). The CIGALE package requires an input file that defines “modules” for fitting along with initial guesses for module parameters.

Each parameter is allowed to take values in the provided initial guess array. CIGALE then computes SEDs for all possible combinations of input parameters in the multidimensional grid defined by the input guesses. After computing the χ^2 for all models, CIGALE performs a Bayesian analysis and outputs the fit parameters that correspond to the model with the highest likelihood. In the case of the host galaxy, we made use of the following modules and constraints:

1. A delayed-exponential SFH model with no late burst population.
2. The (49) simple stellar population with Chabrier initial mass function and metallicity allowed to vary from $0.005Z_{\odot}$ to $2.55Z_{\odot}$.
3. The (50) dust extinction model with extinction computed for the DES g and r bands.
4. The (51) dust emission model with an AGN fraction $f_{\text{AGN}} \leq 0.05$.

The galaxy is not detected in existing near or far-infrared datasets (e.g. WISE) and therefore the dust emission is poorly constrained. CIGALE’s results are summarised in Table S4 including the estimated stellar mass $M_{*,\text{host}} = 10^{9.4\pm 0.19}M_{\odot}$, star-formation rate $\text{SFR} = 0.4 \pm 0.6M_{\odot} \text{ yr}^{-1}$, and internal reddening $E(B - V) = 0.15 \pm 0.08 \text{ mag}$. The large uncertainties arise from the degeneracies that are inherent to SED modeling (e.g. constraining a large number of fitting parameters with relatively few data points).

Our FORS2 spectrum also permits a spectral analysis to assess the galaxy’s stellar population and its associated nebular emission. We analyzed these data with the pPXF software package (52) and a portion of the best-fit model is shown in Fig. S2. The signal-to-noise of these data are too low to provide precise constraints on the stellar population, nevertheless the estimated mass-to-light ratio is consistent with that derived from the photometry. From the observed line fluxes (Table S6), we assess the nature of the nebular line-emission from the galaxy. Unfortunately, the $\text{H}\alpha$ and $[\text{NII}]$ lines lie at $\approx 9700\text{\AA}$ where telluric absorption is

substantial, especially at the high airmass of the observations. We have therefore inflated the uncertainty estimates to $3 \times 10^{-17} \text{ erg s}^{-1} \text{ cm}^{-2} \text{ Ang}^{-1}$. Placing the [OIII]/H β and [NII]/H α line-ratios on the Baldwin-Phillips-Terlevich (BPT) diagram yields an inconclusive result, although the more precise [OIII]/H β ratio implies a lower metallicity galaxy which is consistent with its low stellar mass. The large systematic uncertainty in the H α flux also precludes a precise estimate of the internal extinction from the measured Balmer line ratios. Instead, we adopt the $E(B - V) = 0.15 \text{ mag}$ derived from the photometric analysis (Table S4). From the H β luminosity (Table S6), we estimate the star-formation rate, $\text{SFR}_\beta = 0.6 M_\odot \text{ yr}^{-1}$, consistent with the estimate from photometry.

Fig. S3 places the host galaxy in context with the other three well-studied FRB host galaxies (33, 56, 57), and the general population of $z \sim 0.3$ galaxies (58). We find that the host galaxy has a mass intermediate between the hosts of FRB 1211102 and FRB 180924 and that it lies on the locus of star-forming galaxies. Therefore, our observations disfavor models that invoke dwarf galaxies as the dominant host of FRBs, and also scenarios dominated by super-luminous supernovae usually found in low luminosity/metallicity galaxies (59).

S1.6 Associating FRB 181112 with DES J214923.66–525815.28

While FRB 181112 appears to be associated with DES J214923.66–525815.28 based on the localization, it is possible that this is simply a chance alignment on the sky. To explore this possibility, we have estimated the probability of a chance alignment as follows.

We take a set of 100 random 1 sq. deg. patches of sky within the DES DR1 field and cover it with a uniform square grid with 1'' spacing. We then compute the fraction of the grid with centers that fall within 1'' of a cataloged DES galaxy with $r < 22 \text{ mag}$. This fraction has an average value of 0.31% (see Fig. S4). The chance of randomly finding two such FRB-host pairs with ASKAP (FRB181112, presented here, and FRB180924, from (33)) is therefore

on the order of 10^{-5} . We conclude that FRB 181112 is associated with the luminous galaxy DESJ214923.66–525815.28.

S1.7 Properties of FG-181112

Similar to the host galaxy, we have performed an SED analysis of FG-181112 from the collated photometry (Table S3). We used the same modules as in the case of the host but allowed a maximum AGN fraction of 0.1. The best-fit model is shown in Fig. S5 and summarized in Table 1. The results indicate a massive galaxy ($\log_{10} M_{\star}/M_{\odot} = 10.69^{+0.22}_{-0.46}$), with internal reddening $E(B - V) = 0.43 \pm 0.19$ mag, and a high metallicity $Z_{\text{fg}} = 1.94 Z_{\odot}$ with Z_{\odot} the solar metallicity.

The optical spectrum (Fig. S6) was further analyzed with the pPXF software package (52) to perform line-flux measurements (including the effects of Balmer absorption) and to assess the underlying stellar population. This analysis, summarized in Table 1, yields an estimate of $E(B - V) = 0.07 \pm 0.2$ and a metallicity $Z_{\text{fg}} = 1.62 Z_{\odot}$ (relative to Solar).

The line flux ratios of [OIII]/H β and [NII]/H α place this galaxy in the Seyfert regime of the BPT diagram (Fig. S7), and we place an upper limit on the SFR based on the Balmer-corrected H α flux of $\text{SFR}_{\alpha} < 0.27 M_{\odot} \text{yr}^{-1}$ (see also Table 1). We used this upper bound to constrain our CIGALE analysis.

S1.8 Morphology of the Host and the Foreground galaxies

Sérsic profile fits in the *I*-band image were made of the host and foreground galaxies simultaneously because of their proximity in the sky. The fits were made using GALFIT (60) assuming three components: (i) a constant sky background, (ii) a Sérsic profile for the foreground galaxy and (iii) a Sérsic profile for the host galaxy. The point-spread function (PSF) was estimated from unsaturated sources consistent with circular images using the photutils package (61).

The results of the fitting are shown in Fig. S8 and listed in Table S7. Inputs to GALFIT include an estimate of the PSF, the image, and a list of components (with initial guesses for parameters) to be fitted. GALFIT obtains the best fitting parameters in the minimum χ^2 sense. The parameters are sensitive to the fitting area, especially the Sérsic indices of the two galaxies. In the case of an isolated galaxy, as the area increases, GALFIT tends to assign higher indices i.e. steeper profiles until a critical area beyond which it plateaus. This steady value is accepted as the light profile’s true index.

There is, however, a certain degree of systematic uncertainty involved. One cannot simply increase the fitting area indefinitely, and usually one encounters other objects and must terminate the fitting process. We varied the fitting area to see how the parameter values are affected and we are confident that the fitted uncertainties quoted by GALFIT adequately bound the values. The PA derived indicates the sightline to FRB 181112 occurs approximately along the major axis of FG-181112.

S2 Supplementary Text

S2.1 The DM of FRB181112

The intersection of an FRB sightline with a foreground, massive galactic halo is expected to be a rare occurrence. Applying standard techniques (62) based on the redshift and stellar mass, we estimate the galaxy’s dark matter halo mass to be $M_{\text{halo}} \sim 10^{12.3} M_{\odot}$. Adopting the mass function from the Aemulus simulations (63), the comoving number density of such halos with $M \geq M_{\text{halo}}$ at $z = 0.367$ is $n(M \geq M_{\text{halo}}; z = 0.367) \approx 10^{-3} \text{ Mpc}^{-3}$. The probability to intersect any such halo per absorption length dX within an impact parameter $R_{\perp} \leq 29 \text{ kpc}$ is

$$\ell(X) = \frac{c}{H_0} n \pi R_{\perp}^2 \tag{S14}$$

with H_0 Hubble's constant, c the speed of light, n the number density of halos with $M > M_{\text{halo}}$ in comoving units and R_{\perp} in physical units, and

$$dX \equiv \frac{H_0}{H(z)} (1+z)^2 dz \quad . \quad (\text{S15})$$

Integrating $\ell(X)dX$ from $z = 0$ to 0.47550, we obtain the mean number of halos within the volume of interest (assuming these are randomly distributed). Then, from Poisson statistics, we estimate the chance of intersecting one halo to be $\approx 0.5\%$.

Given the rarity of this event and the high mass of FG-181112, one might expect its halo gas to dominate the dispersion measure DM_{FRB} of the FRB. To explore this hypothesis, we have constructed a DM probability distribution function (PDF) for a set of 10,000 FRBs at $z_{\text{FRB}} = 0.47550$ following the formalism of (18). Specifically, we have assumed the Galactic interstellar medium (ISM) contributes $\text{DM}_{\text{ISM}} = 42 \text{ pc cm}^{-3}$ (64), the Galactic halo contributes $\text{DM}_{\text{MW,halo}} = 60 \text{ pc cm}^{-3}$ (18), and the host contributes $\text{DM}_{\text{host}} = 32 \text{ pc cm}^{-3}$ (this assumes an intrinsic host ISM + halo DM of 50 before evaluating it at $z_{\text{FRB}} = 0.47550$). For the cosmic contribution (the intergalactic medium IGM plus intervening halos) to DM_{FRB} , we have assumed that galactic halos with $M_{\text{halo}} \geq 10^{11} M_{\odot}$ have retained $f_b = 0.75$ of the cosmic fraction of baryons (and 0% otherwise) as an ionized halo gas, and that these are distributed with a modified Navarro-Frenk-White profile (65) (mNFW, with $\alpha = 2, y_0 = 2$; see (18)). This means that approximately half of the baryons today are locked in galactic halos and the remaining fraction f_{IGM} is located in the more diffuse IGM. We may express the DM for the diffuse IGM as:

$$\text{DM}_{\text{IGM}} = \int ds f_{\text{IGM}} \bar{n}_e / (1+z) \quad (\text{S16})$$

where $\bar{n}_e = \rho_b(z) \mu_e / \mu_m m_p$ and where $f_{\text{IGM}}(z)$ is the fraction of cosmic baryons in the diffuse IGM, $\rho_b \equiv \Omega_b \rho_c$, and $\mu_m = 1.3$ and $\mu_e = 1.1667$ account for the mass and electrons of Helium (18). We then generated random realizations of halos foreground to FRB 181112 and

created the PDF shown in Fig. S9. It is evident that the DM of FRB 181112 – corrected for the Galactic ISM, Galactic halo, and host galaxy – lies below the median value of the PDF, i.e. it is not an anomalously high DM event.

This conclusion is further illustrated in Fig. S10 which shows the integrated DM for FRB 181112 from Earth to the event. For the cosmic DM, we have only included DM_{IGM} and our estimate for the DM of FG-181112’s halo. The latter assumes $M_{\text{halo}} = 10^{12.3}M_{\odot}$, $R_{\perp} = 29$ kpc, $f_b = 0.75$, and the modified NFW profile yielding $DM_{\text{FG}} = 122 \text{ pc cm}^{-3}$ after down-weighting by $(1 + z_{\text{fg}})^{-1}$. This analysis suggest that there need not be any additional massive halos in the foreground of FRB 181112 that contribute to DM_{FRB} . The halo gas model adopted in the analysis (mNFW) assumes a higher baryon fraction (f_b) retained in galactic halos than results from some numerical simulations (e.g. (66)). Adopting the (66) density profile scaled to a halo with $M_{\text{halo}} = 10^{12.3}M_{\odot}$ gives $DM_{\text{FG}} \approx 50 \text{ pc cm}^{-3}$. Adopting this value does not qualitatively modify any of the above conclusions but does suggest there are additional halos contributing modestly to DM_{FRB} . Halo gas models with lower f_b imply larger f_{IGM} such that the DM_{cosmic} values are nearly invariant.

The line of sight towards FRB 181112 also intersects the edge of the southern Fermi Bubble of our Galaxy (67), as depicted in Fig. S11. The Fermi Bubbles are plumes of magnetized plasma emanating from the Milky Way’s Galactic Center (67), and are known to host a large mass of cool and ionized entrained material originating in the Milky Way’s nuclear wind (68, 69). Thus, the DM along this direction will include an additional contribution from the Fermi Bubbles. Following (68), we estimate the path length of FRB 181112 through the Fermi Bubbles and estimate the DM contribution towards FRB 181112 as $DM_{\text{FB}} < 5 \left(\frac{n_e}{10^{-3} \text{ cm}^{-3}} \right) \text{ pc cm}^{-3}$. Even for a sightline that passes through the center of the Fermi Bubbles, we predict only a moderate contribution of $DM_{\text{FB}} \sim 20 \left(\frac{n_e}{10^{-3} \text{ cm}^{-3}} \right) \text{ pc cm}^{-3}$. Such a small contribution will be immeasurable in individual FRB sightlines. Estimates for the magnetic field of the Fermi Bub-

bles (70) are sufficiently large to account for the observed rotation measure of FRB 181112.

S2.2 Rotation Measure and a limit on B_{\parallel} for FG-181112

From the measured rotation measure of FRB 181112 ($\text{RM} = 10.9 \pm 0.9 \text{ rad m}^{-2}$), we set an upper limit to the organized magnetic field in FG-181112. In the following we adopt $\text{RM} < 10.9 \text{ rad m}^{-2}$ for the field associated with FG-181112 because our Galaxy including the Fermi Bubbles (§ S2.1) contributes to the measured signal. The former is estimate to be $\text{RM}_{\text{Galactic}} = -2 \pm 11 \text{ rad m}^{-2}$ along the sightline to FRB 181112 (71).

The equation relating RM and B_{\parallel} is:

$$\text{RM} = \frac{e^3}{2\pi m_e^2 c^4} \int B_{\parallel} n_e ds / (1+z)^2 = 8.12 \times 10^2 \text{ rad m}^{-2} \frac{B_{\parallel}}{(1+z)^2} \int n_e ds , \quad (\text{S17})$$

where the latter expression assumes a constant magnetic field and the units for the quantities are μG for B_{\parallel} , cm^{-3} for n_e , and kpc for ds . For the density integral, we consider several models for the gas in galactic halos. Specifically, we take the NFW, mNFW ($\alpha = 2, \gamma_0 = 2$), (72), (66), and (10) models described in (18). These span a range of assumptions on the fraction of baryons retained within galactic halos f_b and the density profile $n_e(r)$. Scaling to our estimated halo mass for FG-181112 of $M_{\text{halo}} = 10^{12.3} M_{\odot}$, we calculate $\int n_e ds$ over an interval $\pm 15 \text{ kpc}$ and $\pm r_{\text{vir}}$ at $R_{\perp} = 29 \text{ kpc}$. The former, corresponding to $L = 30 \text{ kpc}$ (as assumed in the main text), encompasses the majority of the gas and minimizes assumptions related to the outer halo. We also note that typical values for n_e near the effective mid-plane of these models are $\approx 10^{-3} \text{ cm}^{-3}$ (also the fiducial value adopted in the main text). Inverting equation S17 we derive estimates for $B_{\parallel}^{\text{max}}$, the maximum allowed organized magnetic field (ignoring any field reversals). These are illustrated in Fig. S12 for the suite of models considered. These values are lower than previous estimations for halo gas (22) and far lower than measurements from regions above the plane of disks in nearby galaxies (e.g. (73)).

S2.3 Scattering Analysis

At cosmological distances the characteristic temporal broadening time due to the multipath propagation caused by scattering in an inhomogeneous plasma is (23)

$$\tau = \frac{1}{ck} \left(\frac{r_F}{r_{\text{diff}}} \right)^2 = \frac{D_L D_{LS} \lambda_0}{2\pi c k D_S (1 + z_L) r_{\text{diff}}^2}. \quad (\text{S18})$$

with D the angular diameter distance to the source (S), screen (L), or the screen to the source (LS), z_L is the redshift to the screen, r_{diff} is the diffractive scale, and where $k = 2\pi/\lambda_0$ and λ_0 is the wavelength in the observer frame. For a power-law power spectrum of density inhomogeneities with index β between an inner scale l_0 and outer scale L_0 , r_{diff} is the point at which the phase structure function (23),

$$D_\phi(r) = \begin{cases} 2^{4-\beta} \pi^2 r_e^2 l_0^{\beta-4} \text{SM} \frac{\lambda_0^2}{(1+z_L)^2} \Gamma\left(2 - \frac{\beta}{2}\right) r^2, & r < l_0, \\ \frac{2^{5-\beta}}{\beta-2} \pi^2 r_e^2 \text{SM} \frac{\lambda_0^2}{(1+z_L)^2} \frac{\Gamma(2-\beta/2)}{\Gamma(\beta/2)} r^{\beta-2}, & r \gg l_0, \end{cases} \quad (\text{S19})$$

satisfies $D_\phi(r) = 1$. Here, $\text{SM} = \int dz C_N^2(z)$ is the scattering measure of the scattering medium (see, e.g. (74)), C_N is the amplitude of turbulence per unit length, and r_e is the classical electron radius. The value $\beta = 11/3$, corresponding to Kolmogorov turbulence, is often found to apply to turbulent plasma in the interstellar medium (75).

For scattering on a single thin plane, the pulse broadening kernel follows, to a good approximation, the function $P_D(t) = \exp(-t/\tau_{\text{scatt}})$. The pulse broadening time, τ_{scatt} , is observationally referenced to the time at which the pulse falls to e^{-1} of its maximum value. (76) shows that this occurs approximately at $\tau_{\text{scatt}} \equiv (3/2)\tau$ (noting the factor of 1/2 difference between τ above and the definition of t_D in (76)).

For the geometry applicable to scattering by the foreground galaxy, one has $D_S = 1.23$ Gpc, $D_L = 1.05$ Gpc and $D_{LS} = 0.26$ Gpc. For the scattering time to fall below $\tau_{\text{scatt}} < 40 \mu\text{s}$ at 1300 MHz along this line of sight requires a value of $r_{\text{diff}} > 9.2 \times 10^{10}$ cm in any inhomogeneous plasma located within the environs of the foreground galaxy.

The diffractive scale, the length scale between adjacent ray paths over which the medium induces one radian of phase difference, is evaluated from the scattering timescale for the geometry relevant to FG-181112; attributing all the scattering along this line of sight to this galaxy yields a minimum estimate of its scattering strength. Assuming the diffractive scale to lie outside the inner scale of the turbulence (i.e. the dissipation scale; typical values are 200-1000 km for Galactic interstellar turbulence), and that the density fluctuations follow a Kolmogorov spectrum, $\beta = 11/3$, one has $r_{\text{diff}} > 9.2 \times 10^{10}$ cm and $\text{SM} < 5.6 \times 10^{13} \text{ m}^{-17/3}$. We estimate the total variance in the column density (i.e. the variance in the dispersion measure) in the medium using the fact that the value of the phase structure function at the outer scale of the turbulence is twice the phase variance, $D_\phi(L_0) = 2\langle\Delta\phi^2\rangle$, and $\Delta\phi = r_e[\lambda_0/(1+z_L)]\text{DM}$. For the value of SM derived above the root mean square of the column density variations implied by the scattering is:

$$\langle(\Delta\text{DM})^2\rangle^{1/2} < 0.089 \left(\frac{L_0}{1 \text{ pc}}\right)^{5/6} \text{ pc cm}^{-3}, \quad (\text{S20})$$

where we have normalised to a fiducial value of $L_0 = 1$ pc, noting that this outer scale is most plausibly also the scale at which the turbulence is driven.

The estimate of the column density variance is the most basic result derivable involving the fewest number of unknown parameters (to wit, the outer turbulent scale). However, if the thickness of the medium is known one may obtain the variance in the in-situ electron density n_e . For a scattering medium thickness of ΔL , in which the average value of $C_N^2(z)$ is uniform throughout the medium, one has $C_N^2 < 3.7 \times 10^{-8} (\Delta L/50 \text{ kpc})^{-1} \text{ m}^{-20/3}$. For density fluctuations whose variance on the outer scale is $\alpha^2\langle n_e\rangle^2$, where $\langle n_e\rangle$ is the mean density, one has ((24)) $C_N^2 = 0.066\alpha^2\langle n_e\rangle^2 L_0^{-2/3}$. For the value of C_N^2 derived here, the upper limit on the electron density is

$$\langle n_e\rangle < 2.3 \times 10^{-4} \alpha^{-1} \left(\frac{L_0}{1 \text{ pc}}\right)^{1/3} \left(\frac{\Delta L}{50 \text{ kpc}}\right)^{-1/2} \text{ cm}^{-3}. \quad (\text{S21})$$

These limits apply irrespective of whether the baryons in the plasma of the foreground galaxy are smoothly distributed (where geometric optics would suffice to treat the problem) or whether they are inhomogeneous on scales smaller than the Fresnel scale (hence diffraction occurs). The limit on r_{diff} is still well below the Fresnel scale of $r_{\text{F}} = 5.1 \times 10^{13}$ cm (i.e. the Fresnel scale exceeds the limit on the diffractive scale by a factor of 540, so diffractive theory is applicable here). Indeed, irrespective of whether the radiation propagates through smooth lensing structures on scales above r_{F} , the absence of diffractive scattering and temporal smearing in the medium nonetheless yields a valid upper limit on the root-mean-square column density variations in the medium, subject to the assumption that the density fluctuations follow a power law power spectrum.

Were the phase to be smooth on scales comparable to r_{F} (i.e. for a lensing formulation to be readily applicable), the root mean square DM fluctuations would be less than $4.7 \times 10^{-4} (L_0/1 \text{ pc})^{5/6} \text{ pc cm}^{-3}$ and the limit on the in-situ electron density would be

$$\langle n_e \rangle < 1.2 \times 10^{-6} \alpha^{-1} \left(\frac{L_0}{1 \text{ pc}} \right)^{1/3} \left(\frac{\Delta L}{50 \text{ kpc}} \right)^{-1/2} \text{ cm}^{-3}. \quad (\text{S22})$$

S2.3.1 Interpretation of scattering constraint

Our analysis of scattering is via equation (S22). This formula constrains the level of turbulence both in hot virialized gas and in colder 10^4 K gas. Our measurement of the scatter broadening, τ , also constrains the refractive scattering of a cool population of parsec-scale clouds as has been hypothesized (25). In what follows we discuss how our constraint pertains to these different scenarios.

Turbulence in hot virialized gas

The canonical picture is that massive dark matter halos with mass M_{halo} are filled with virialized gas at virial temperature $T_{\text{vir}} \approx 10^6 \text{ K} [M_{\text{halo}}/(10^{12} M_{\odot})]^{2/3} (1+z)$ with a filling factor of nearly unity. This gas is stirred on kiloparsec scales by galactic winds, AGN-driven bubbles,

and inflows, with observations suggesting a mach number $\mathcal{M} \approx 1$ on ~ 10 kpc scales (6, 77). This stirring drives a turbulent cascade that, if the electron density fluctuations follow the spectrum of Kolmogorov turbulence to $r_{\text{diff}} \sim 10^{10}$ cm, leads to the scattering constraint represented by equation (1). Here we discuss whether these assumptions are likely to hold.

There are multiple effects that can suppress the cascade on scales larger than $r_{\text{diff}} \sim 10^{10}$ cm (78). The amplitude of density fluctuations responsible for scattering may be suppressed if the gas can cool for eddies with size $\ell > L_{\text{MHD}}$, where $L_{\text{MHD}} \sim L_0 \beta^{-3/2}$ is the scale where the magnetic energy density becomes larger than the turbulent kinetic energy and β is the ratio of thermal to magnetic pressure. (Below L_{MHD} the isobaric component of these larger-scale density fluctuations are passively mixed by the incompressive shear Alfvén waves that characterize magnetohydrodynamic turbulence, generating small-scale density fluctuations (78, 79). If the turbulence is isothermal at L_{MHD} , then there are no density fluctuations to mix.) For virialized gas, the cooling time is expected to be $\gtrsim 10$ times longer than sound crossing time on the halo scale to avoid strong thermal instability (80) and so the turbulence should be adiabatic. The turbulent cascade could be terminated on sufficiently small scales by collisions with neutrals or ions (78). However, we find that there are insufficient neutrals for the former damping mechanism to be effective (as the virialized CGM is highly collisionally ionized). For ion diffusion, eddies with turnover time equal to the proton diffusion time are damped (78), corresponding to

$$\ell_0^{\text{pd}} \sim 6 \times 10^{13} \text{ cm} \left(\frac{1 \text{ kpc}}{L_0} \right)^{1/2} \left(\frac{10^{-4} \text{ cm}^{-3}}{n_e/\beta} \right)^{3/2}. \quad (\text{S23})$$

The value $\ell_0^{\text{pd}} = 6 \times 10^{13}$ cm is several orders of magnitude larger than r_{diff} assumed by our constraint, weakening our constraint on $\langle n_e \rangle$ by $\sim (r_{\text{diff}}/\ell_0^{\text{pd}})^{1/6}$ (eqn. S19); this translates into a suppression by factor of a few. Furthermore, electron diffusion can damp fluctuations on a scale, which (78) estimates will damp the density fluctuations by a factor of $\beta^{-1/2}$ on the somewhat larger scale of $\sqrt{m_p/m_e} \ell_{\text{in}}^{\text{pd}}$, where m_p and m_e are the electron and proton masses.

Turbulence in 10^4K gas

If not in the virialized phase, intrahalo gas is most likely to be in a denser, $T \sim 10^4\text{K}$ photoionized phase. Observations suggest volume filling fractions of $f_V \sim 10^{-3} - 10^{-2}$ for halos of similar masses to FG-181112 (6, 25), with the latter corresponding to a mass fraction of 0.5 in the cold phase. Despite this phase likely having $f_V \ll 1$, its higher density and potentially smaller driving scale for turbulence may allow it to dominate the scattering. We can re-write equation (1) rescaled to values that are more relevant for this case:

$$\left(\frac{\langle n_e \rangle}{0.1 \text{ cm}^{-3}}\right) \left(\frac{f_V}{10^{-3}}\right)^{1/2} < 0.6 \alpha_{\text{rms}}^{-1} \left(\frac{\Delta L}{50 \text{ kpc}}\right)^{-1/2} \left(\frac{L_0}{1 \text{ kpc}}\right)^{1/3} \left(\frac{\tau_{\text{scatt}}}{40 \mu\text{s}}\right)^{5/12} \text{ cm}^{-3}, \quad (\text{S24})$$

where we have explicitly stated a volume filling fraction that was previously incorporated into our definition in our α so that $\alpha = \alpha_{\text{rms}} f_V^{1/2}$. The fiducial value of $\langle n_e \rangle = 10^{-1} \text{ cm}^{-3}$ is based on pressure equilibrium with the virialized gas assuming $T = 3 \times 10^6\text{K}$ (in accord with that expected for FG-181112) and $n_{e,\text{vir}} = 0.3 \times 10^{-3} \text{ cm}^{-3}$ – roughly the minimum of the circumgalactic medium (CGM) models considered in Fig. S12 at 30 kpc. This formula suggests $f_V \sim 10^{-3}$ for $L_0 \sim 1 \text{ kpc}$. The constraints are an order of magnitude stronger if we assume $L_0 \sim 1 \text{ pc}$, as might be the case if thermal instability drives the turbulence (25). Our formula for the scattering timescale from Kolmogorov turbulence is nearly identical (with slight differences in normalization) to that for parsec-scale clouds presented in (81). Self-shielding of the metagalactic ionizing background should start to diminish the electron fraction for $\left(\frac{\langle n_e \rangle}{0.1 \text{ cm}^{-3}}\right) \left(\frac{f_V}{10^{-3}} \frac{\Delta L}{50 \text{ kpc}}\right)^{1/2} \gtrsim 1$ at $z = 0.37$, somewhat larger than the values we are able to rule out for the fiducial numbers in equation (S24).

Let us now consider whether the density fluctuations associated with the turbulent cascade may be suppressed in the cold 10^4K clouds, which would weaken our constraints on $\langle n_e \rangle$. Following (78), below the cooling scale $L_c \equiv (c_s t_{\text{cool}})^{3/2} L_0^{-1/2}$ where $c_s t_{\text{cool}} \sim 1 n_e^{-1} \text{ pc}$ (25) is the distance a sound wave travels with speed c_s in a cooling time t_{cool} , the turbulence is nearly

isothermal, suppressing small-scale density fluctuations from passive mixing as described for the previous scenario. Assuming that this is larger than L_{MHD} (requiring $L_0 < 1 \text{ pc } n_e^{-1} \beta^{3/2}$), density fluctuations will be instead sourced by either slow waves or passively mixing Reynolds stresses present at $\gtrsim L_{\text{MHD}}$. The density fluctuations from slow waves are suppressed by a factor of $\beta^{-1/2}$ relative to hydrodynamic scales; our result that the large-scale magnetic field is below equipartition suggests a suppression. For eddies with $\ell < L_{\text{MHD}}$, density fluctuations sourced by Reynolds stresses are suppressed by the factor $\sqrt{c_s t_{\text{cool}}/L_0}$ relative to the Kolmogorov extrapolation (78). Thus, for driving on parsec scales, suppression of the cascade may not be expected. However, for kiloparsec-scale driving (for which Reynold stresses contribute negligibly to the small-scale density variations), the amplitude of density fluctuations in the cascade is not suppressed if $\beta \sim 1$ or if $L_c < L_{\text{MHD}}$. Otherwise a suppression with $\alpha \propto \beta^{-1/2}$ is expected. We again expect proton diffusion to cutoff the cascade, but the higher densities of the cold gas make this cutoff less important than for the virialized gas, especially for kiloparsec driving scales (eqn. S23). In conclusion, the parameter space for when the turbulent cascade in the cold gas is suppressed is complex.

A refractive parsec-scale cloud population

Motivated by indications that there exists a population of cold parsec-scale clouds in the CGM (25), we consider the scattering of spherical parsec-scale clouds that are not turbulent. Non-turbulent clouds might occur if they survive quiescently for many sound crossing times after they are produced, as hypothesized in (25). (If turbulently driven on the cloud scale [with an undamped cascade to r_{diff}] the scatter broadening yields the limit given by eqn. S24 with L_0 being the cloud size (81).) Here we briefly sketch the derivation of refractive time delays for spherical clouds of size R . While a spherical cloud is certainly an idealization, additional cloud structure will only increase the amount of scattering. We also consider the generalisation to a range of cloud sizes.

For a single cloud at $r \ll R$, we can expand the phase structure function in a power series $D_\phi^{\text{cl}}(r) = \phi_0^2 r^2 / R^2 + \dots$, where ϕ_0 is a constant characteristic phase, using that the phase structure function must be zero at $r = 0$ and an even function in r . Calculating τ_{scatt} requires $D_\phi^{\text{cl}}(r)$ only for $r \ll R$, so that retaining just the first term in the power series is a sufficient approximation. For spatially uncorrelated clouds with an average of N intersected across the halo, the full structure function is $D_\phi(r) = ND_\phi^{\text{cl}}(r)$. The diffractive scale is defined as $D_\phi(r_{\text{diff}})/2 = 1$ such that $r_{\text{diff}} = \sqrt{2/N}R/\phi_0$. When we take ϕ_0 to be the phase across the center of the cloud, the resulting expression for the scattering angle from this r_{diff} is identical to that calculated for refractive clouds ((82); section 11.4), using a different method. A numerical calculation shows that ϕ_0 is 2.2 times larger than the phase across the cloud center. We used Monte-Carlo integration to verify our form for D_ϕ and measure its normalization. The extreme curvature at the edge of our idealization of perfectly spherical, tophat clouds means that the integral to compute ϕ_0 needs to be regulated to yield a convergent answer. We find that D_ϕ changes little if we do not include sightlines that fall with rarity of a part in 10^4 or instead 10^5 from the cloud edge, much larger than the N expected physically in the picture of (25).

The scatter broadening time τ_{scatt} can be calculated from r_{diff} using equation (S18); it yields a smaller τ_{scatt} than the case where the clouds are fully turbulent (eqn. S24) and that reported in (81) whose results we interpret as being appropriate for fully turbulent clouds. However, before we interpret this refractive delay as scatter broadening, we must check whether multi-path propagation is expected. There would only be multi-path propagation if the size of the scattering surface χ is $\gtrsim R$ so that an independent set of structures is intersected, where $\chi^2 = 2c\tau_{\text{scatt}}D_L D_{LS} / [D_S(1 + z_L)]$. For the angular diameter distances and redshift of FG-181112, $\chi = 0.011 \text{ pc} \times \sqrt{\tau_{\text{scatt}} / (40 \mu\text{s})}$, smaller than the parsec estimate for circumgalactic cloud sizes (25). Taking this criterion into account, our constraint on the refractive scattering of spherical

clouds is

$$\left(\frac{n_e}{0.1 \text{ cm}^{-3}}\right) \left(\frac{\Delta L}{50 \text{ kpc}} \frac{f_V}{10^{-3}} \frac{0.1 \text{ pc}}{R}\right)^{1/2} < 0.2 \left(\frac{\tau_{\text{scatt}}}{40 \mu\text{s}}\right)^{1/2} \quad \text{if} \quad R \lesssim 0.011 \text{ pc} \left(\frac{\tau_{\text{scatt}}}{40 \mu\text{s}}\right)^{1/2};$$

$$\left(\frac{n_e}{0.1 \text{ cm}^{-3}}\right) \left(\frac{\Delta L}{50 \text{ kpc}} \frac{f_V}{10^{-3}}\right)^{1/2} \left(\frac{0.1 \text{ pc}}{R}\right)^{3/2} < 1.6 \quad \text{otherwise,} \quad (\text{S25})$$

although again self-shielding also limits the maximum $n_e^2 f_V \Delta L$ probed by scattering (see above). The former equation applies for bubbles whose size is small enough to generate multiple extrema in phase, and the latter weaker constraint applies to larger bubbles (as we require a higher column to result in scatter broadening from multipath propagation). While weaker than the model in (81), which assumed a structure function with the scaling of Kolmogorov turbulence, these constraints show that even a tiny volume filling factor of $f_V \sim 10^{-3}$ for ~ 0.1 pc clouds – about the scale anticipated in (25) – is ruled out in FG-181112. While we have made the assumption of a single cloud radius, the radius only enters our calculation for τ_{scatt} via its dependence on N , the number of clouds intersected, as long as the clouds are sufficiently small to contribute to multipath propagation.

S2.3.2 Other galaxy halo constraints from scattering

Here we compare the limits obtained in this section with those deduced for other galaxies.

M31: The properties of the baryonic halo of M31 are constrained by angular broadening measurements of distant radio galaxies in the background of this galaxy obtained using widefield very long baseline interferometry (VLBI) at a 1640 MHz (83). These observations detect angular broadening of ≈ 15 milliarcseconds towards the centre of the galaxy, at a projected distance of 0.25 kpc, which is attributed to an extreme scattering environment close to the centre of this galaxy. However, some background radio sources at separations between 15 and 30 arcmin of the galaxy center possess angular sizes < 1 mas, thus placing an upper limit on the ionized baryons present both in the disk and halo of M31 through which the background radiation prop-

agates ((83), their Table 3 and figure 7). (Other sources at similar projected angular distances are resolved but these are attributed to the finite angular sizes of the sources themselves.)

The absence of angular broadening at the 1 mas level immediately places a lower limit on the value of r_{diff} associated with the scattering in the disk+halo of M31 of 7.2×10^6 m. This in turn implies an upper limit on SM of $1.6 \times 10^{17} \text{ m}^{-17/3}$ under the assumption that r_{diff} exceeds the inner scale of the turbulence: no measurement of the frequency dependence of the (absent) angular broadening is available to verify this assumption, however this assumption is supported by measurements of interstellar turbulence in the Milky Way (e.g. (84)). This upper limit in turn implies a limit on the root-mean-square electron column which, expressed in terms of the usual units of dispersion measure, gives

$$\langle \Delta \text{DM}^2 \rangle^{1/2} < 4.7 \left(\frac{L_0}{1 \text{ pc}} \right)^{5/6} \text{ pc cm}^{-3}. \quad (\text{S26})$$

This is an upper limit on the halo baryon contribution in several senses: both because no angular broadening is detected and because any detection would include a contribution from both the disk and the halo of this galaxy.

The Milky Way: Measurements of (or limits on) the angular broadening or pulse broadening from sources located beyond the Milky Way constrain the properties of its ionized baryonic halo. In general, temporal smearing limits are more constraining at low frequencies due to the $\tau_{\text{scatt}} \propto \nu^{-4}$ dependence of the scattering. The most stringent limit is due to the pulse smearing measurement of FRB 170827 (85), from which a smearing time of $4.1 \pm 2.7 \mu\text{s}$ at 842 MHz is deduced from its $\approx 30 \mu\text{s}$ -duration pulse structure (85). The decorrelation bandwidth of the burst structure is 1.5 MHz, which would imply a more stringent limit of $0.8 \mu\text{s}$ on the scattering timescale, but the origin and interpretation of the spectral structure in FRBs is presently less straightforward, so we conservatively use the limit deduced directly from the temporal structure of the FRB itself.

The most conservative limit on the properties of the baryonic halo are derived by attributing all of the observed temporal smearing to our Galaxy (rather than any intermediate system or host galaxy). For a fiducial effective screen distance of $d_{\text{screen}} = 10 d_{10}$ kpc from Earth one derives a diffractive scale length $r_{\text{diff}} = 3.5 \times 10^7 d_{10}^{1/2}$ m and $\text{SM} = 7.6 \times 10^{14} d_{10}^{-5/6} \text{m}^{-17/3}$ and

$$\langle \Delta \text{DM}^2 \rangle^{1/2} < 0.65 \left(\frac{L_0}{1 \text{ pc}} \right)^{5/6} \left(\frac{d_{\text{screen}}}{10 \text{ kpc}} \right)^{-5/12} \text{ pc cm}^{-3}. \quad (\text{S27})$$

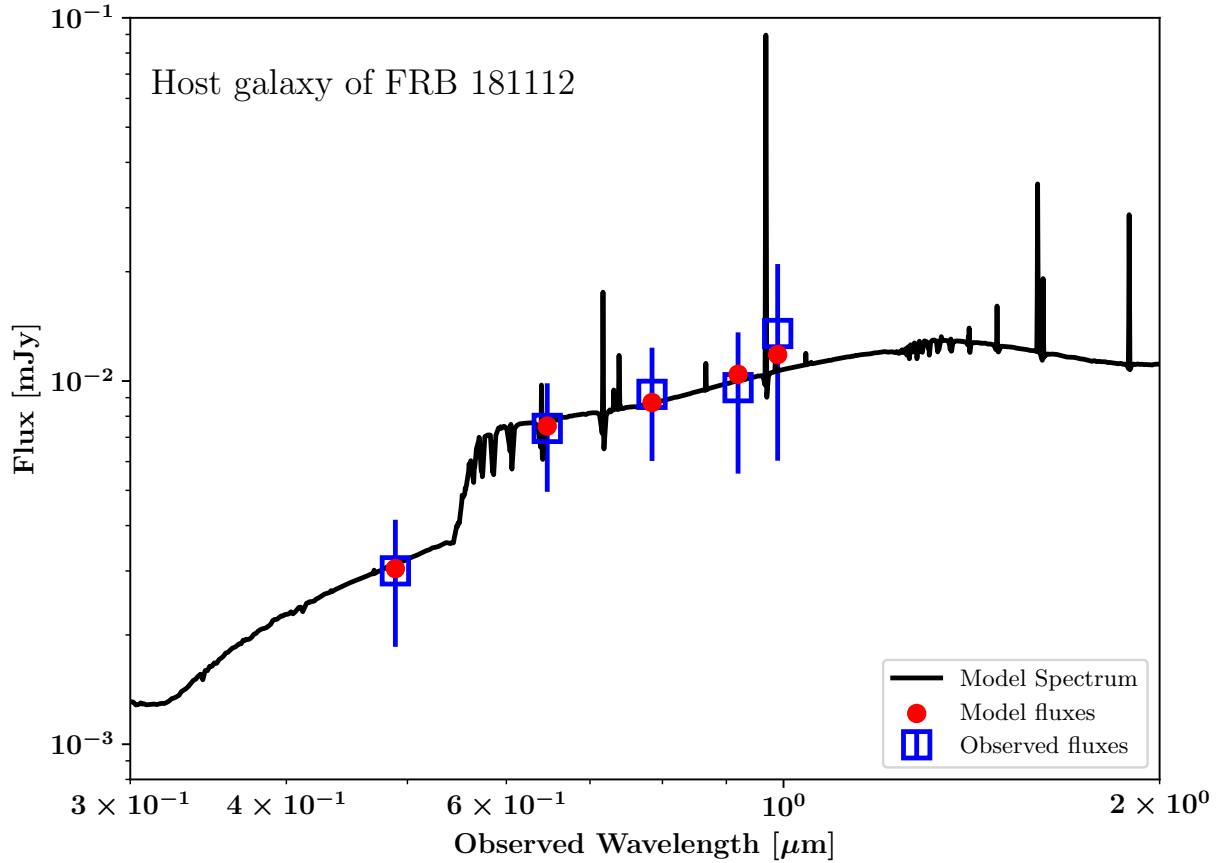


Fig. S1: Spectral energy distribution of the host galaxy of FRB 181112. Comparison of observed fluxes of the host galaxy of FRB 181112 (blue squares) against the best-fit model values (red circles) as derived with the CIGALE software package. The black curve shows the model spectrum. The derived properties (Table S4) include stellar mass $M_* = 10^{10.69} M_\odot$, reddening $E(B - V) = 0.43 \pm 0.19$ mag, and SFR $\approx 0.4 \pm 0.6 M_\odot \text{yr}^{-1}$.

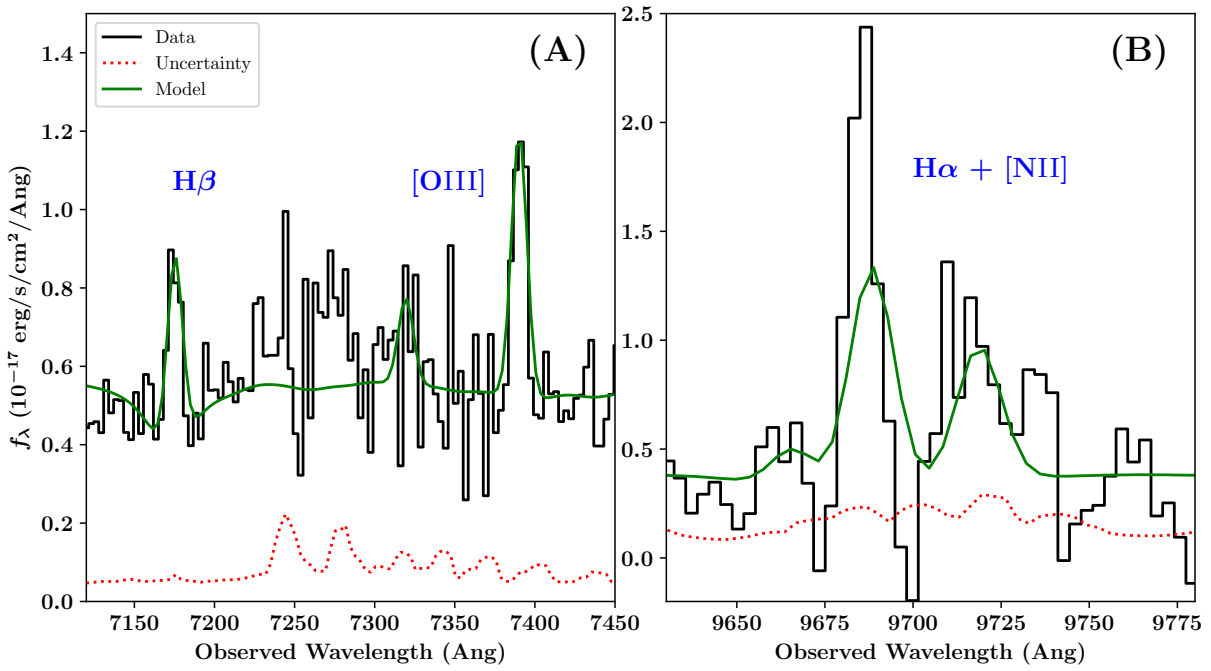


Fig. S2: Fitted profiles to spectral features for the host galaxy of FRB 181112. VLT/FORS2 spectrum (specific flux f_λ ; black histogram) and uncertainty (red dotted line) of several nebular lines from the host galaxy of FRB 181112. The best-fitting model (green solid line) was generated with the pPXF software package, which includes estimates for Balmer absorption. The data at $\lambda \approx 9700\text{Å}$ suffer from substantial telluric absorption which has not been fully corrected.

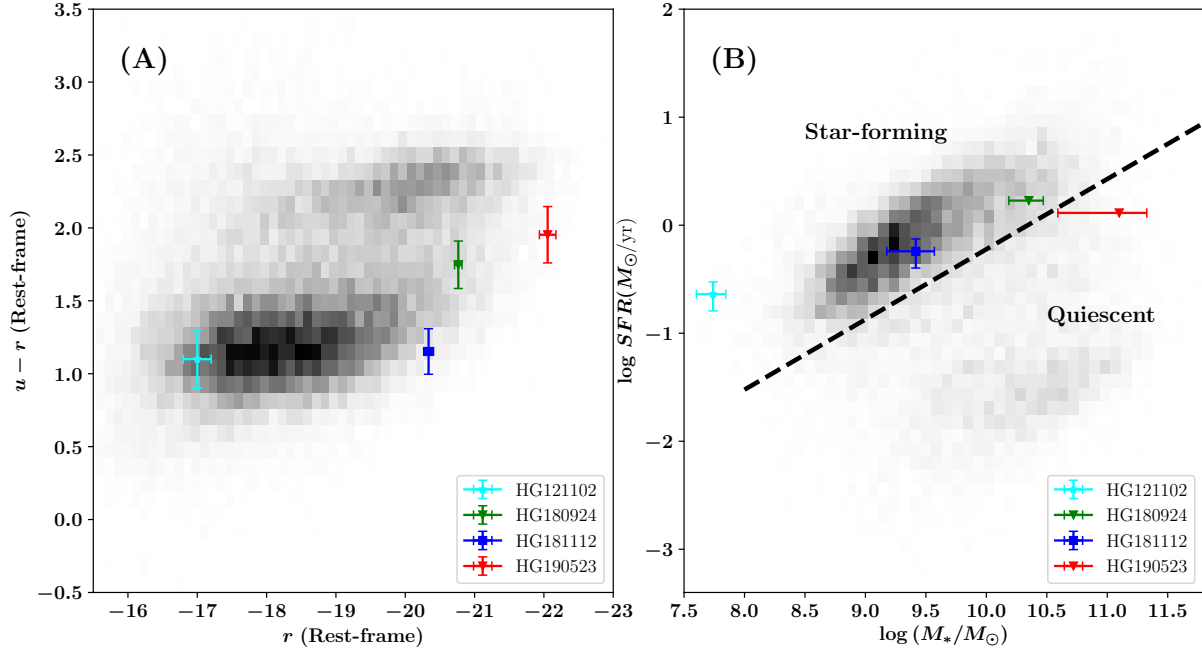


Fig. S3: Comparison of FRB host galaxies with galaxies from the PRIMUS survey (58). Panel A shows a rest-frame color-magnitude diagram comparing galaxy color with luminosity. The PRIMUS sample (gray histogram) shows two main sequences of blue ($u-r \approx 1.1$ mag) and red ($u-r \approx 2.4$ mag) galaxies. Panel B compares galaxy SFRs with stellar mass with the dashed line separating star-forming galaxies from quiescent galaxies. While the host of the Repeater FRB (labelled HG 121102; (56)) occurred in a very faint, blue, and star-forming galaxy, the non-repeating FRBs localized by ASKAP (labelled HG 180924 (33) and HG 181112 (12); thus far non-repeaters) and the Deep Synoptic Array (HG 190523; (57)), have more luminous hosts (panel A). These galaxies also have higher stellar mass (panel B) and show a diversity of SFRs (the downward triangles for HG 180924 and HG 190523 indicate upper limits to the SFR).

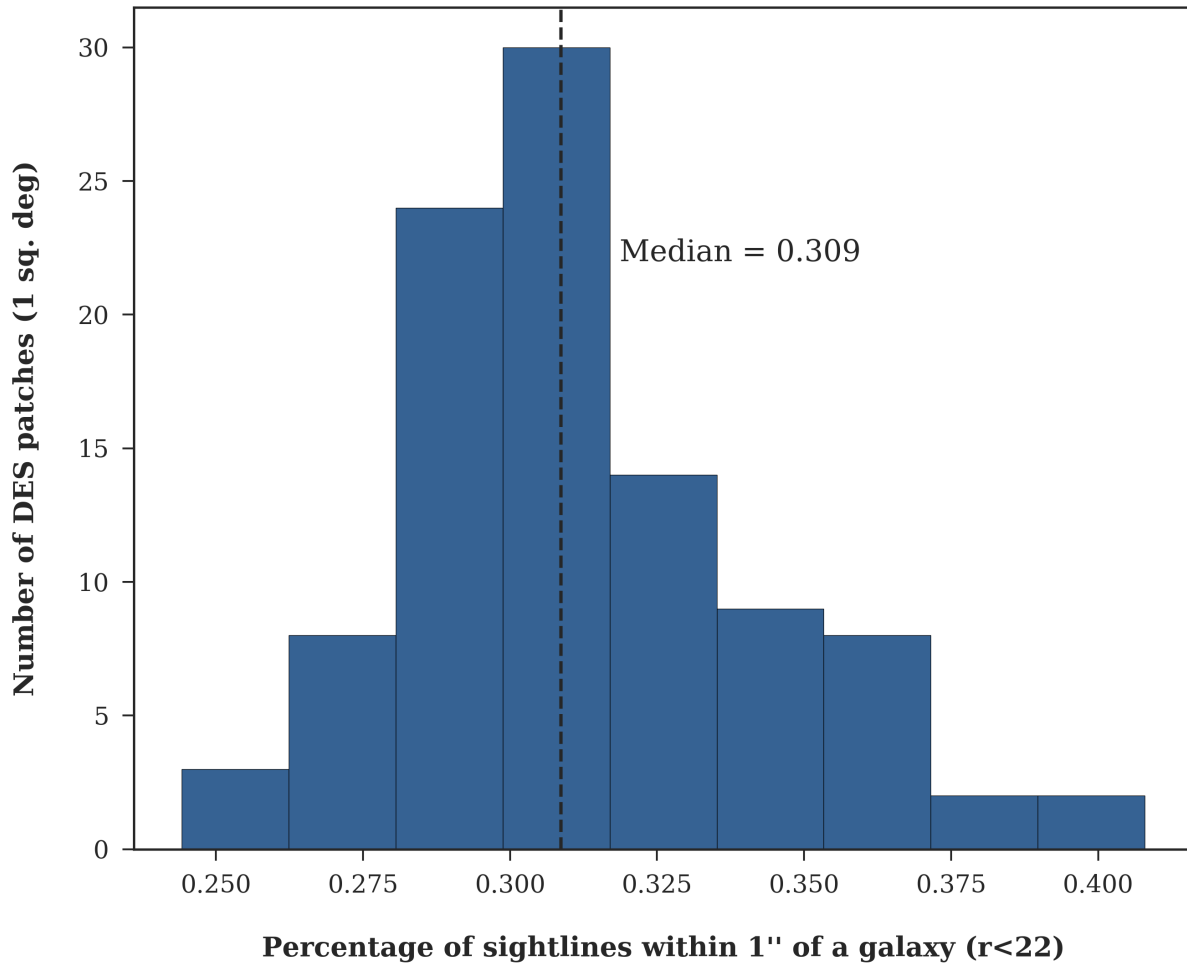


Fig. S4: Probability of a random association with a $r < 22$ mag galaxy. The distribution from 100 trials of the percentage of random sightlines falling within $1''$ of a galaxy with $r < 22$ mag in a random 1 sq. deg patch of sky in the DES-DR1 survey. The dashed black line represents the median value (0.3%) of the full trial set.

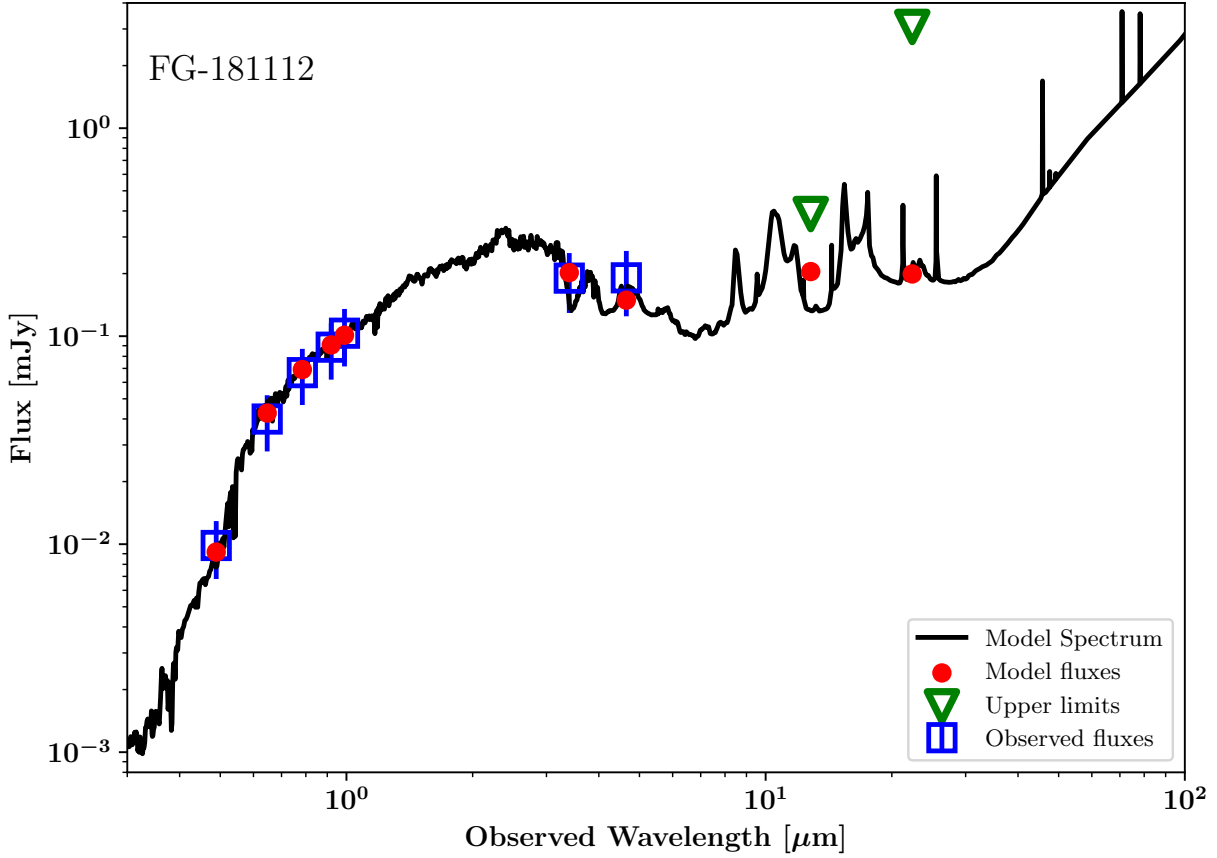


Fig. S5: Spectral energy distribution of the foreground galaxy FG-181112. Comparison of observed fluxes of FG-181112 (blue squares) against the best-fit model values (red circles) as derived with the CIGALE software package. Green triangles represent upper limits on the observed fluxes. The black curve shows the model spectrum. The derived properties include stellar mass $M_* = 10^{10.69} M_\odot$, reddening $E(B - V) = 0.43 \pm 0.19$ mag, and AGN fraction $f_{\text{AGN}} = 0.1$.

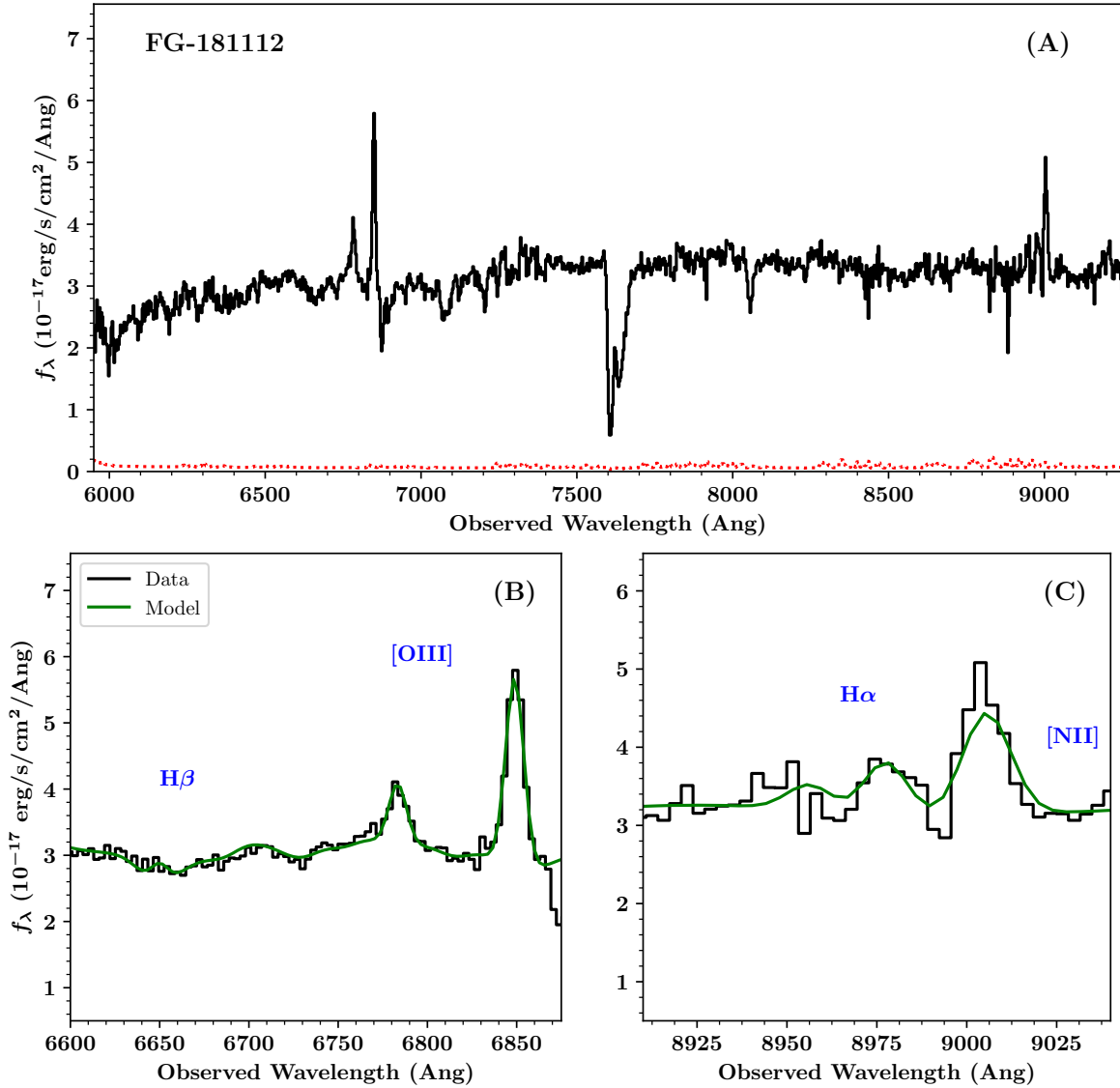


Fig. S6: Optical spectrum of the foreground galaxy FG-181112. (A) VLT/FORS2 spectrum of FG-181112 (black histogram) and estimated uncertainty (red dotted line). The strong absorption feature at $\approx 7600\text{\AA}$ is telluric. (B,C) Zoom-ins on key nebular emission lines fitted using the pPXF software package (green solid line).

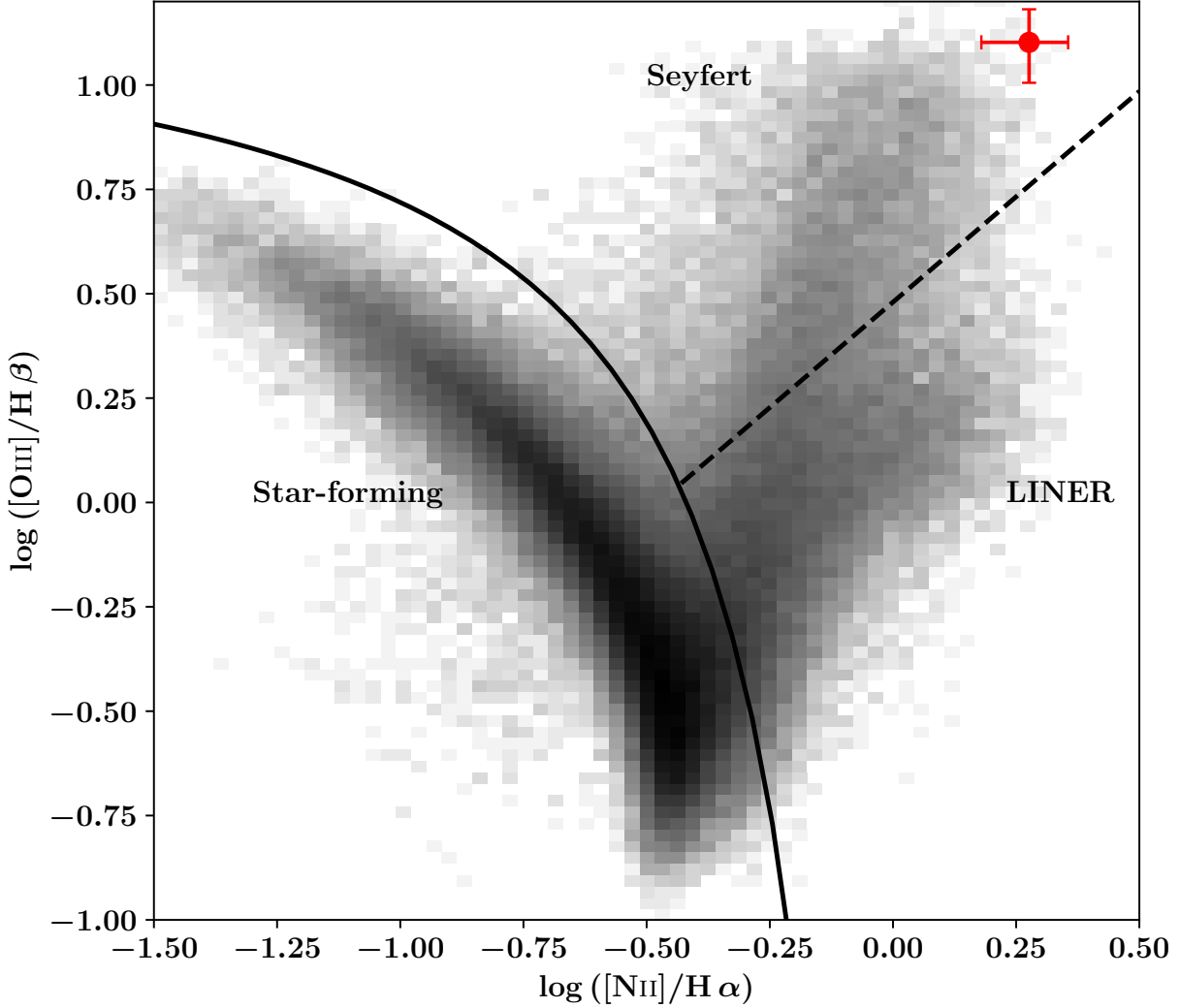


Fig. S7: Diagnostic plot for characterizing emission line galaxies. Grey points show emission line ratios from nearby galaxies ($z = 0.02 - 0.4$) in the Sloan Digital Sky Survey, restricted to have signal-to-noise greater than 5. The intensity scaling is logarithmic to accentuate regions away from the dominant, star-forming locus. Black lines separate star-forming galaxies (solid; (53)) from sources dominated by harder ionizing spectra (54), and the dashed line separates sources designated as Active Galactic Nuclei from Seyfert and low-ionization nuclear emission-line region (LINER) galaxies (55). The line ratios of FG-181112 (red point) show it is a Seyfert galaxy, i.e., it hosts an active galactic nucleus.

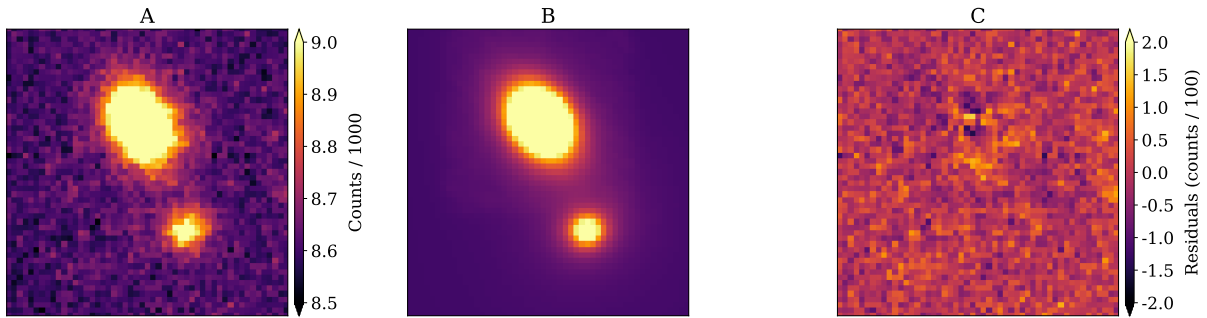


Fig. S8: Morphological analysis of the host and foreground galaxies for FRB 181112. (A) FORS2 *I*-band image of the host (bottom) and foreground (top) galaxies. The image is centered on the coordinates RA, Decl. 21h49m23.8s, $-52^{\circ}58'12.2''$ (J2000), has an angular extent of $12.6''$ on a side, and is oriented with N up and E to the left. (B) Best fit model with three components: two Sérsic profiles and a constant sky background. The color scale is the same as (A). (C) The residuals between the data and the model.

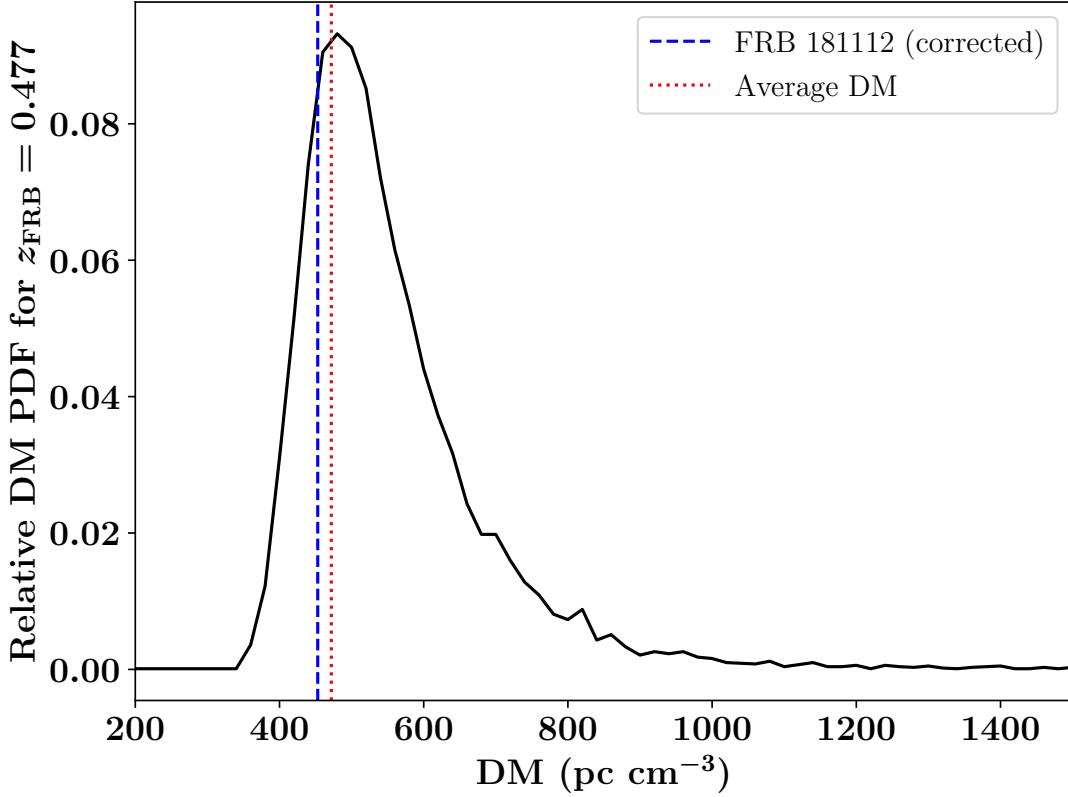


Fig. S9: Comparison of the corrected DM of FRB 181112 with random expectation. The black curve is the estimated PDF for a random sample of FRBs at $z = 0.47550$ using the methodology described in (18). These DM values do not include contributions from our Galaxy nor the host galaxy. The blue dashed vertical line indicates the DM value of FRB 181112 corrected for the Galactic ISM, Galactic halo, and an assumed value for the host galaxy (see text). We find that it lies near the average expected value for an FRB at this redshift (red, dotted line), even though the sightline intersected the halo of FG-181112.

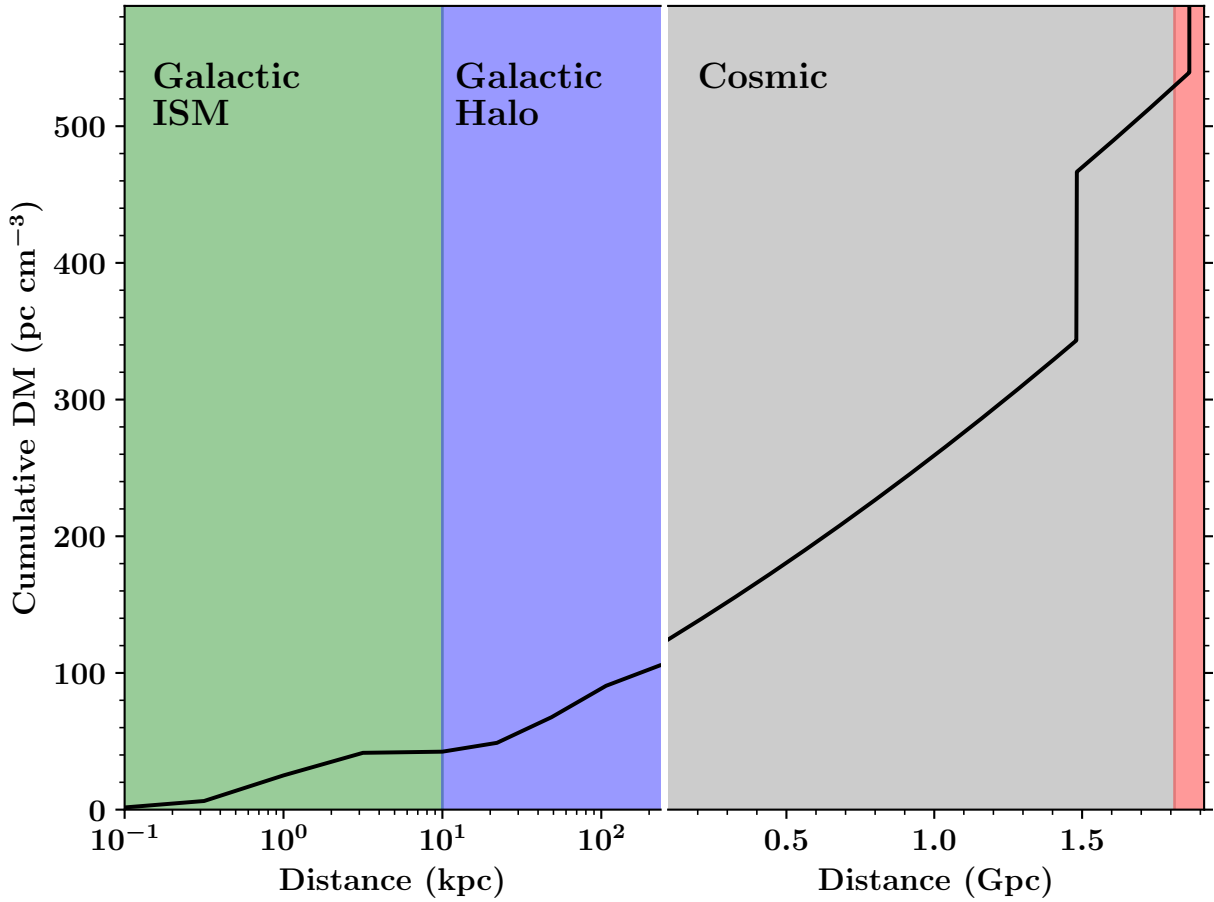


Fig. S10: Diagram of the cumulative DM from Earth to FRB 181112. The cumulative DM (black curve) includes contributions from our Galactic ISM (green), Galactic halo (blue), a restricted cosmic contribution (gray, see text), and the host galaxy (pink). The jump at approximately 1.5 Gpc is due to the intersection with FG-181112’s halo. The y-axis of the figure terminates at the measured $DM_{\text{FRB}} = 589.27 \text{ pc cm}^{-3}$ for FRB 181112. The curve shows that the FRB 181112 sightline is unlikely to have intersected many additional, massive halos.

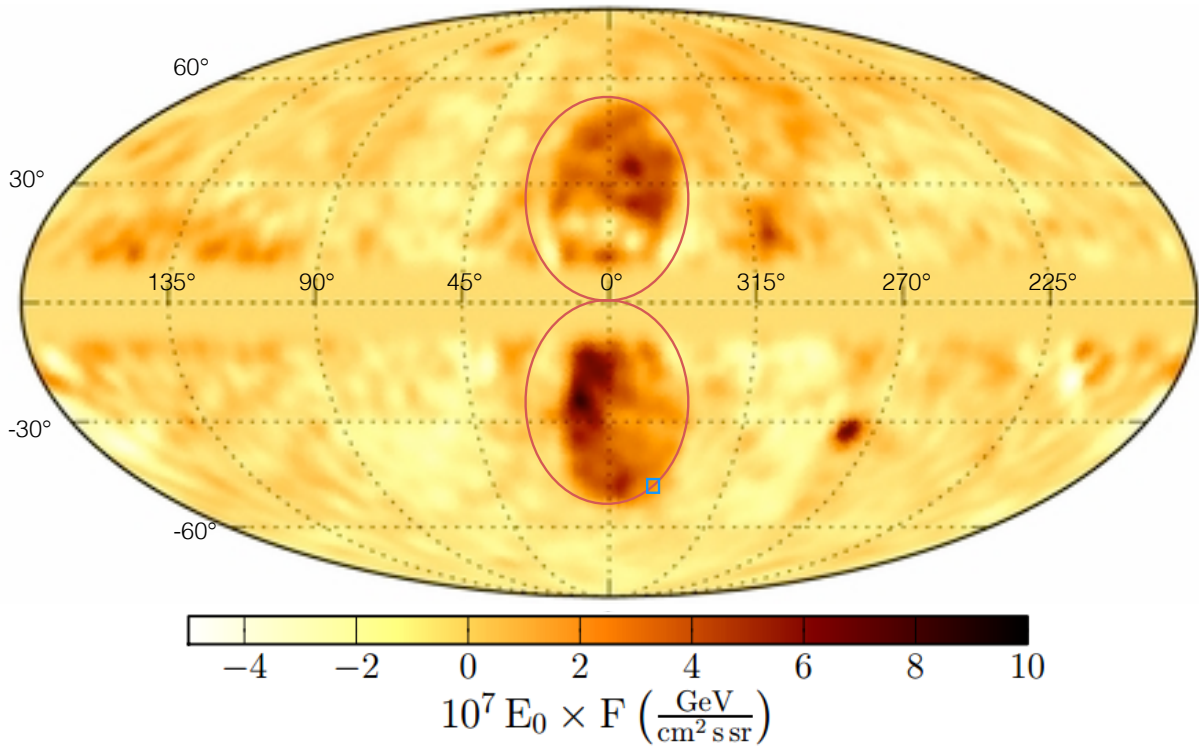


Fig. S11: The sightline to FRB 181112 intersects the southern Fermi bubble. The all-sky Fermi residual gamma-ray intensity map observed in the 3–10 GeV range, in Galactic coordinates centered on the Galactic Center (adapted from (68, 86)). The twin Fermi Bubbles are marked by the red ellipses. The blue square marks the line of sight through the Fermi Bubbles towards FRB 181112, which intersects the edge of the southern bubble.

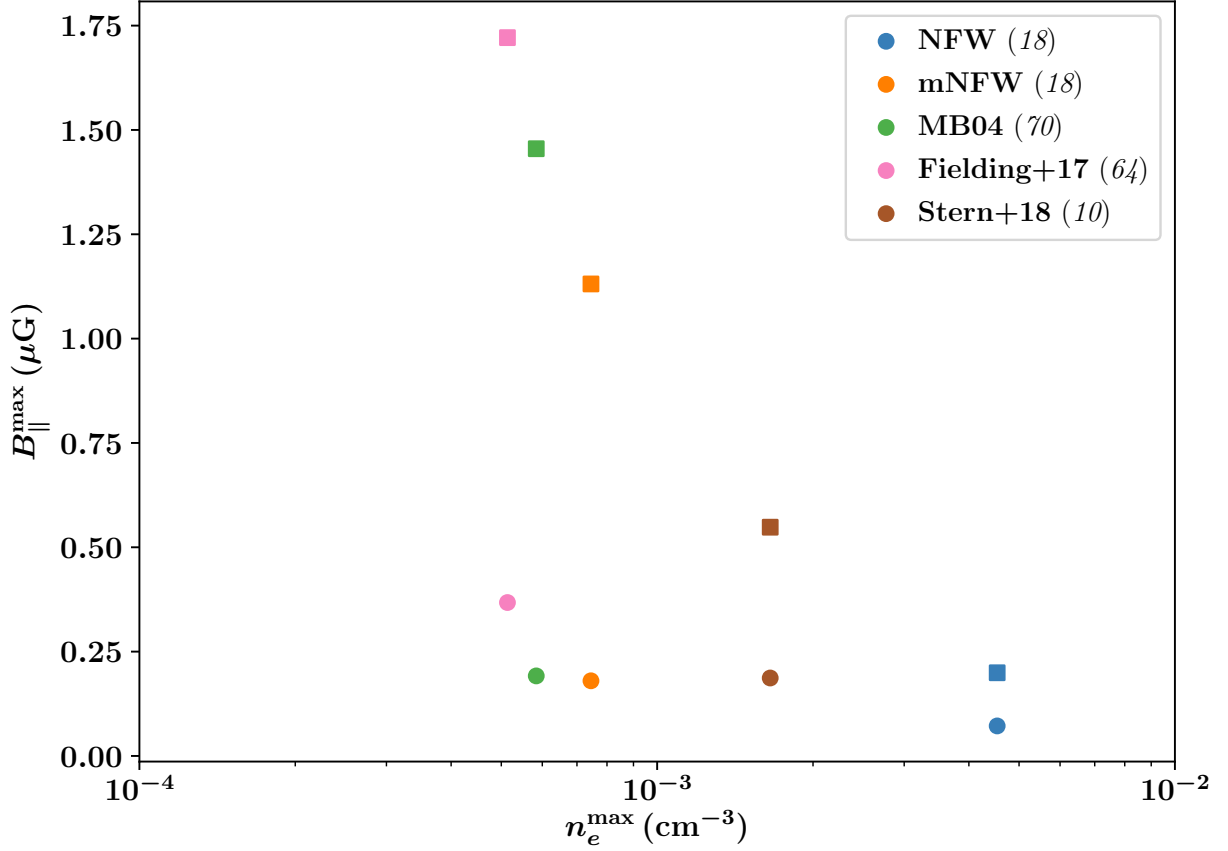


Fig. S12: Upper limits on the organized parallel magnetic field B_{\parallel}^{\max} in the halo of FG-181112 for a series of assumed CGM models. The circles (squares) integrate the rotation measure through the entire halo (or ± 15 kpc from the mid-plane). See § S2.2 and (18) for details on the various CGM models shown. We conclude that the organized magnetic field along the FRB sightline in the halo of FG-181112 is less than $1 \mu\text{G}$ and likely less than $0.3 \mu\text{G}$.

Supplementary Tables

Table S1: **Fitted positions and flux densities of the 3 brightest ASKAP field sources**

Source	RA (J2000)	RA _{uncertainty} (mas)	Dec. (J2000)	Dec. _{uncertainty} (mas)	S (mJy)	S _{uncertainty} (mJy beam ⁻¹)
SUMSS 215155–531646	21:51:55.37	2100	–53:16:47.5	1400.0	40.9	3.8
SUMSS 215036–525538	21:50:37.16	2100	–52:55:40.0	1400.0	33.9	3.8
SUMSS 215606–532916	21:56:06.32	2900	–53:29:11.2	1800.0	29.5	3.7

Table S2: **Phase calibrators used for the ATCA observation. The position of SUMSS 215155–531646 was derived using these calibrators.**

Calibrator (J2000)	Source (J2000)	RA (J2000)	Dec. (J2000)
Calibrators used			
	PKS B2117–642	21:21:55.0217	–64:04:30.042
	PKS B2215–508	22:18:19.0247	–50:38:41.731
FRB 181112 field source			
PKS B2117–642	SUMSS 215155–53164	21:51:55.307	–53:16:46.56
PKS B2215–508	SUMSS 215155–53164	21:51:55.291	–53:16:47.09

Table S3: **Galaxy Photometry.** DES-DR1 photometry were published in (13) and WISE photometry were taken from (41). Uncertainty values of -999.00 indicate upper limits.

Galaxy	Survey	Filter	Value (mag)	Uncertainty (mag)
Host	DES-DR1	g	22.71	0.09
Host	DES-DR1	r	21.73	0.05
Host	DES-DR1	i	21.49	0.06
Host	DES-DR1	z	21.45	0.11
Host	DES-DR1	Y	21.07	0.17
Host	VLT	g	22.57	0.04
Host	VLT	I	21.51	0.04
Foreground	DES-DR1	g	21.42	0.03
Foreground	DES-DR1	r	19.90	0.01
Foreground	DES-DR1	i	19.34	0.01
Foreground	DES-DR1	z	19.03	0.01
Foreground	DES-DR1	Y	18.86	0.02
Foreground	VLT	g	21.20	0.04
Foreground	VLT	I	19.20	0.02
Foreground	WISE	W1	15.53	0.04
Foreground	WISE	W2	14.89	0.06
Foreground	WISE	W3	12.28	-999.00
Foreground	WISE	W4	8.59	-999.00

Table S4: **Physical properties of the host galaxy of FRB 181112 derived from CIGALE and nebular line analysis**

Package	Parameter	Value	Uncertainty	Unit
CIGALE	Stellar Mass	0.26	0.1	$10^{10} M_{\odot}$
CIGALE	AGN Fraction	0.0	0.0	
CIGALE	Rest-frame $u - r$	1.2	0.2	mag
CIGALE	Rest-frame M_r	-20.34	0.07	mag
CIGALE	SFR	0.4	0.6	$M_{\odot} \text{ yr}^{-1}$
CIGALE	$E(B - V)$	0.15	0.08	mag
pPXF	SFR_{β}	0.57	0.17	$M_{\odot} \text{ yr}^{-1}$

Table S5: Physical properties of the foreground galaxy FG-181112 derived from CIGALE and nebular line analysis

Package	Parameter	Value	Uncertainty	Unit
CIGALE	AGN Fraction	0.1	0.2	
CIGALE	Metallicity	0.017	0.016	
CIGALE	Rest-frame $u - r$	2.3	0.1	mag
CIGALE	Rest-frame M_r	-21.98	0.05	mag
pPXF	$E(B - V)$	0.07	0.20	mag
pPXF	[NII]/H α	0.28	0.03	log10
pPXF	[OIII]/H β	1.10	0.05	log10

Table S6: **Emission line fluxes and luminosities for host galaxy and foreground galaxy FG-181112 of FRB 181112 measured from the FORS spectroscopy.** The luminosity values include an extinction correction.

Galaxy	Line	Flux (10^{-17} erg/s/cm ²)	Flux Uncertainty (10^{-17} erg/s/cm ²)	Luminosity ^a (10^{40} erg/s)	Lum. Uncertainty (10^{40} erg/s)
Host	H α	6.4	0.8	5.8	0.7
Host	H β	2.9	0.2	2.6	0.2
Host	H γ	0.7	0.2	0.6	0.2
Host	[NII] 6584	4.9	1.0	4.4	0.9
Host	[OIII] 5007	5.4	0.3	4.9	0.3
Foreground	H α	5.5	0.3	3.4	0.2
Foreground	H β	1.8	0.2	1.2	0.1
Foreground	[NII] 6584	10.5	0.5	6.5	0.3
Foreground	[OIII] 5007	23.0	0.3	15.5	0.2

Table S7: **GALFIT Sérsic profile fits**

Galaxy	Sérsic index	Index fit uncertainty	Half-light radius (arcsec)	Half-light radius uncertainty (arcsec)
Host	1.9	0.4	0.64	0.04
Foreground	2.48	0.08	0.760	0.008